Journal of Nuclear Medicine, published on December 29, 2022 as doi:10.2967/jnumed.122.264433

Submillimeter resolution positron emission tomography for high-sensitivity mouse brain imaging

Han Gyu Kang[1], Hideaki Tashima[1], Hidekatsu Wakizaka[1], Fumihiko Nishikido[1], Makoto Higuchi[2], Miwako Takahashi[1], Taiga Yamaya[1]

[1]Department of Advanced Nuclear Science, National Institutes for Quantum Science and Technology (QST), 4-9-1, Anagawa, Inage-ku, Chiba, Japan

[2]Department of Functional Brain Imaging, National Institutes for Quantum Science and Technology (QST), 4-9-1, Anagawa, Inage-ku, Chiba, Japan

Corresponding author:

Han Gyu Kang, PhD

National Institutes for Quantum Science and Technology (QST), 4-9-1, Anagawa, Inage-ku, Chiba, Japan

Tel: +81-43-382-3702; Fax: +81-43-206-0819; e-mail: kang.hangyu@qst.go.jp

Running title: Ultrahigh resolution small animal PET

Key Words Submillimeter resolution, Preclinical positron emission tomography, Depth-of-interaction, In vivo mouse brain imaging;

Immediate Open Access: Creative Commons Attribution 4.0 International License (CC BY) allows users to share and adapt with attribution, excluding materials credited to previous publications.

License: https://creativecommons.org/licenses/by/4.0/.

Details: https://jnm.snmjournals.org/page/permissions.

ABSTRACT

Positron emission tomography (PET) is a powerful molecular imaging technique that can provide functional information of living objects. However, the spatial resolution of PET imaging has been limited to around 1 mm which makes it difficult to visualize mouse brain function in detail. Here we report an ultrahigh resolution small animal PET scanner we developed that can provide a resolution approaching 0.6 mm to visualize mouse brain function with unprecedented detail.

Methods: The ultrahigh resolution small animal PET scanner had an inner diameter of 52.5 mm and axial coverage of 51.5 mm. The PET scanner consisted of 4 rings each of which had 16 depth-of-interaction (DOI) detectors. Each DOI detector consisted of a 3-layer staggered lutetium yttrium orthosilicate crystal array with a pitch of 1 mm and 4×4 SiPM array. The physical performance was evaluated in accordance with the National Electrical Manufacturers Association NU4 protocol. The spatial resolution was evaluated with various resolution phantoms. In vivo glucose metabolism imaging of mouse brain was performed.

Results: The peak absolute sensitivity was 2.84% with an energy window of 400-600 keV. The 0.55 mm rod structure of a resolution phantom was resolved using an iterative algorithm. In vivo mouse brain imaging with ^{18}F-FDG showed clear identification of cortex, thalamus, and hypothalamus which were barely distinguishable in a commercial preclinical PET scanner that we used for imaging comparison.

Conclusion: The ultrahigh resolution small animal PET scanner is a promising molecular imaging tool for neuroscience research using rodent models.

INTRODUCTION

In vivo imaging of rodent models is crucial to understand the underlying mechanisms of various human diseases such as cancer (*1,2*) and neurodegenerative diseases (*3,4*); in turn, this understanding can lead to the discovery of new drugs for human diseases. Positron emission tomography (PET) has been playing a distinctive role in preclinical research as a molecular imaging tool that provides spatiotemporal information on biochemical processes of living animals (*5*). Small animal PET imaging is particularly useful to discover and assess specific biomarkers of cancer and neurodegenerative diseases at a measurable picomolar level.

However, the spatial resolution of commercial PET scanners (*6-9*) has been limited around 1.0-1.3 mm which cannot distinguish small imaging objects like mouse brain whose substructural organs (e.g. cortex, thalamus) are located near each other on the order of a few hundred micrometers. Even the state-of-the art small animal PET scanners developed since late 2020 by laboratories (*10-14*) and companies (*15-18*), the spatial resolutions are still around 0.8-1.2 mm and not good enough to identify small mouse brain structures in detail, which makes it difficult to assess subtle alterations of mouse brain activity in neurodegenerative disease models.

One of the major factors that limits the spatial resolution of small animal PET scanners is the crystal pitch which typically ranges from 1.2 mm to 1.6 mm (*19*). A second factor is depth-of-interaction (DOI) information which can preserve the spatial resolution in a small ring diameter geometry where the resolution blurring by the photon non-collinearity effect is relatively small (*20*). Inter-crystal scattering (ICS) is a third factor that degrades the spatial

resolution by assigning the line-of-response (LOR) to the wrong crystal positions especially in finely pixelated crystal arrays (*21*).

In this study, we develop an ultrahigh resolution small animal PET scanner that addressed these technical issues to provide submillimter resolution in a 51.5 mm long axial coverage. The silicon photomultiplier (SiPM) based staggered 3-layer DOI detector (*22*) was used to build the PET scanner for submillimeter in vivo rodent brain imaging.

MATERIALS AND METHODS

Submillimeter resolution small animal PET scanner

The developed submillimeter resolution small animal PET scanner (hereafter referred to SR-PET) had four rings of 16 DOI detectors each, thereby resulting 52.5 mm inner diameter and 51.5 mm axial FOV (Fig. 1A). Each DOI detector (*22*) consisted of a 3-layer lutetium yttrium orthosilicate (LYSO) crystal array (EPIC Crystal), a 1 mm thick acrylic light guide, and an SiPM 4×4 array (S14161-3050HS-04; Hamamatsu Photonics K. K.,) (Fig. 1B and Supplemental Video 1). The 3-layer LYSO crystal array consisted of the 1st (10×9), 2nd (10×10), and 3rd (11×11) layers stacked in a staggered configuration with an offset of crystal half pitch in radial and axial directions to encode the DOI information in the crystal map (Supplemental Fig. 1). The crystal thicknesses of the 1st, 2nd, and 3rd layers were 4 mm, 4 mm and 7 mm, respectively. The LYSO crystals (0.9×0.9 mm^2 cross section) were optically isolated using a 0.1 mm thick $BaSO_4$ powder layer resulting in a 1 mm crystal pitch. Each crystal layer was optically coupled using epoxy glue (refractive index = 1.52; EPO-TEK® 301-1; Epoxy Technology). Then the 3-layer LYSO crystal array, light guide and SiPM were

optically coupled by using room temperature vulcanizing silicon rubber (refractive index = 1.45; KE420; Shin-Etsu Chemical Co., Ltd.). The top surface of the 1st crystal layer was covered by two layers of Teflon tape with a total thickness of 0.2 mm. The radial gap distances between the detector blocks were 1.42 mm, 2.0 mm, and 2.58 mm, for the 1st, 2nd and 3rd layers, respectively (Fig. 1A). Four LYSO crystal arrays were mounted on the SiPM with a spacing of 13.5 mm in axial direction (Fig. 1B). A cylindrical light tight cover was used to block the external light.

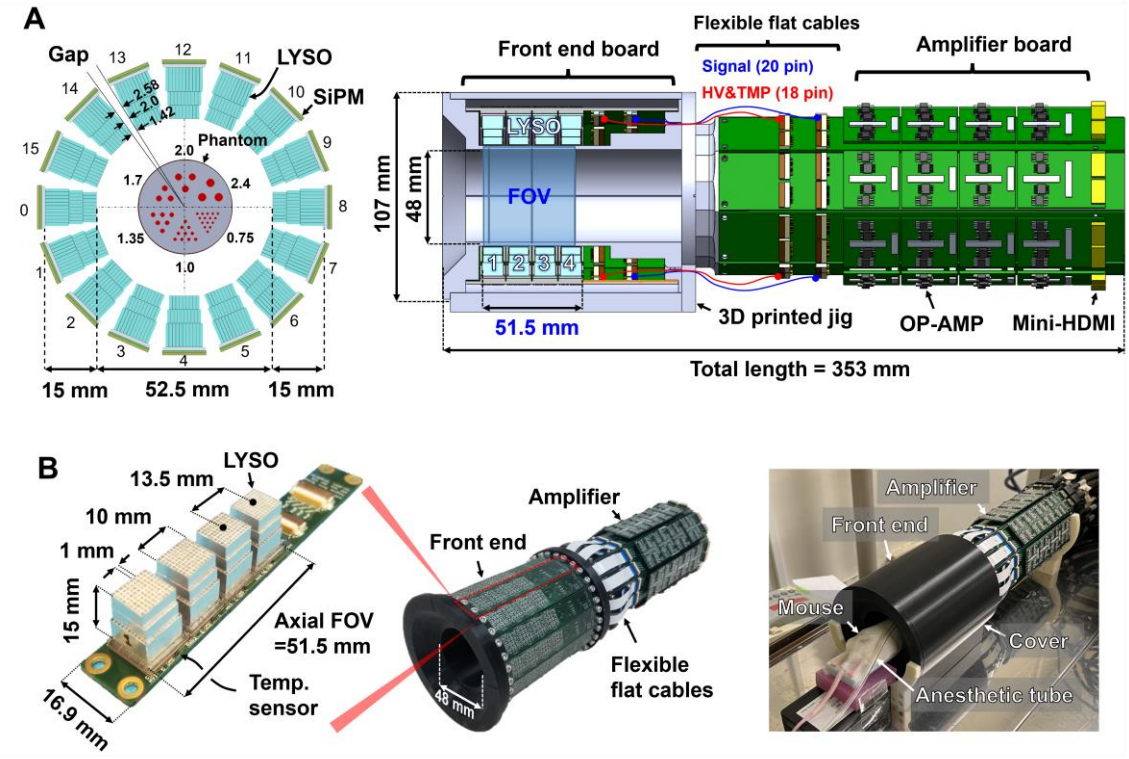

Fig. 1. (A) Schematic drawings of the SR-PET scanner in front and side views. (B) Photos of the SR-PET scanner with one of the front-end boards, and in vivo mouse imaging setup with the PET scanner.

For the SiPM signal readout and amplifications, custom-made front-end and amplifier

boards were used (Supplemental Fig. 2A). A front-end board had four SiPMs which were mounted with a central pitch of 13.5 mm in the axial direction (Supplemental Fig. 2B). The SiPM bias voltage of +41.0 V (over-voltage = 3.2 V) was applied to the common cathode (Supplemental Fig. 2C). Sixteen anode signals of each SiPM were reduced into four positional signals by using a resistive network (Supplemental Fig. 2D). The positional signals from the front-end board were transferred to the amplifier boards through 10 cm long flat flexible cables. A timing signal which also carried the energy information was generated by summing the four positional signals. Each amplifier board consisted of four add-on amplifier boards, and each add-on board could process 10 analog signals from two DOI detectors (Supplemental Fig. 2E).

The positional signals were amplified by using a low power quad-channel amplifier (OPA4684IPWT; Analog Device). The timing signal was fed to a fast amplifier (AD8000; Analog Device), then a pole-zero-cancellation circuit was used to obtain fast pulse rise (26 ns) and decay times (144 ns) (Supplemental Fig. 2F). The temperature of each SiPM was monitored by a temperature sensor (LM94023; Texas Instruments) attached near the SiPM. The SiPM ambient temperature was maintained at 26±0.4°C by an air conditioner in the experimental room to minimize the SiPM gain drift owing to the temperature change. No temperature compensation technique was used for the SiPM since the maximum variation of the ambient temperature was only within ± 0.4 °C. The amplified SiPM analog signals from each amplifier board were transferred to a custom-made interface board via four 3 m long high-definition multimedia interface cables (Supplemental Fig. 3). Subsequently, the SiPM signals were sent to a custom-made data acquisition (DAQ) system (*23*) via four 1.8 m long

radiofrequency shielded cables (Hewtech). The 320 channel 8-bit DAQ system was used to digitize the SiPM analog signals with a sampling rate of 50 MSPS and an integration time of 250 ns.

The list-mode PET data were acquired in the singles mode and then stored on a hard disk of a desktop personal computer. Subsequently, the prompt coincidence events were identified by using coincidence processing software with a coincidence window of 10 ns. The random coincidence events were recorded by a delayed coincidence window with a time offset of 260 ns.

The normalization data were obtained for 72 h by rotating a 0.16 MBq ^{68}Ge-^{68}Ga line source (diameter, 2 mm; length, 260 mm) by using a motor stage (SGSP-80YAW; Sigmakoki) with a rotating radius of 22.5 mm.

Image reconstruction

For image reconstruction, analytical and iterative algorithms were used, namely, the 2D filtered-back-projection (FBP) and list-mode 3D ordered-subset-expectation-maximization (OSEM) algorithms. The voxel size of 0.25×0.25×0.25 mm^3, and matrix size of 200×200×206 were used for the image reconstruction. For the 2D FBP algorithm, oblique sinograms were rebinned into direct sinograms by using the single-slice rebinning (SSRB) algorithm (*24*), then were reconstructed with a gap filling method (*22*) which did not degrade the spatial resolution (Supplemental Fig. 4).

For the list-mode 3D OSEM algorithm, the detector response function modeling and normalization factors were incorporated into the system matrix. The system matrix was

computed using the Siddon ray tracing algorithm with five sub-divided crystal positions for each crystal layer (*22*). The 8 subsets and 10 iterations were used unless otherwise specified. A 3D Gaussian image domain blurring (IDB) was incorporated during the image reconstruction to smooth the reconstructed images. The iteration number and IDB kernel size (i.e. FWHM) were determined by visual check depending on the imaging object (Supplemental Table. 1). For PET data correction, the normalization and random correction were performed. Scatter and attenuation corrections were not used. For all the reconstructed PET images, the contrast was adjusted only for the maximum level while the minimum level was set to be zero without any adjustment.

Physical performance evaluation

The physical performance of the SR-PET scanner was evaluated based on the National Electrical Manufacturers Association (NEMA) protocol. To evaluate the spatial resolution and sensitivity, a NEMA ^{22}Na point source (Eckert & Ziegler Isotope Products) with a diameter of 0.25 mm and an activity of 0.26 MBq was used.

The energy resolution and coincidence timing resolution were evaluated with the ^{68}Ge line source positioned at the center of the FOV. A Voronoi diagram was applied to a crystal map to extract the energy information of individual crystals (*22,25*). Subsequently, a global energy spectrum was generated by summing all the energy spectra of 64 DOI detectors after photo-peak alignment for the individual crystals. Then system energy resolution was calculated by the ratio of full width at half maximum (FWHM) to the photo-peak position without applying the SiPM saturation correction (*22*). A global timing spectrum was obtained from the

timestamp information of the 64 DOI detectors with an energy window of 400-600 keV after time skew correction (*23*).

The axial sensitivity profile was obtained by translating the ^{22}Na point source with a step distance of 0.5 mm (crystal half pitch) from -26.5 mm to 26.5 mm. The PET data were taken for 1 min for each axial position. The ^{176}Lu intrinsic radioactivity and the positron branching ratio of the ^{22}Na source (i.e. 0.91) was taken into account for the sensitivity calculation.

The spatial resolution was measured using the ^{22}Na point source from the center to the 15 mm radial offset position with a step distance of 2.5 mm (Supplemental Fig. 5A). In addition, the spatial resolution was measured at different axial offset positions of 6.25 mm, 13.5 mm, and 19.75 mm, respectively with an interval of 6.25 mm corresponding to the half pitch of the ring (Supplemental Fig. 5B). The list-mode PET data were reconstructed using the 2D FBP algorithm without any gap filling method. Iterative algorithms can artificially enhance spatial resolution for point source in air especially with extremely high iterations (*26*). Therefore, we chose 10 iterations for OSEM where the radial full width at tenth maximum (FWTM) improvement reached a plateau and the radial FWHM improvement had not reached its plateau yet (Supplemental Fig. 6). A line profile was extracted from the reconstructed PET image, then the FWHM and FWTM were evaluated. The energy window of 440-560 keV was used and the ^{22}Na point source diameter of 0.25 mm was not subtracted from the spatial resolution.

The count rate performance was evaluated with a 70 mm long cylindrical NEMA mouse-like phantom (diameter, 25 mm). A 60 mm long tubing source containing ^{18}F solution (initial activity, 18.2 MBq) was inserted into the 3.2 mm diameter hole of the phantom. The PET

data were acquired for 1 min every 30 min, until the activity decreased to 0.02 MBq. The true, scatter, random, and noise equivalent count rate (NECR) were calculated with different energy windows of 250-750 keV, 350-650 keV, 400-600 keV, and 440-560 keV (*22*).

To evaluate the recovery coefficient, spill-over ratios, and uniformity, a NEMA NU4 image quality phantom was filled with ^{18}F-FDG of 1.7 MBq and then scanned for 180 min. The energy window of 400-600 keV was used. For the OSEM algorithm, the IDB kernel size of 1.25 mm was used without applying any post-processing filter. For the FBP algorithm, the gap filling method was applied followed by 3D Gaussian post-processing filtering with a kernel size of 1 mm. The recovery coefficient, spill-over ratios, and uniformity were calculated from the axially summed images with a 10 mm slice thickness.

Resolution phantom imaging

The spatial resolution of the PET scanner was evaluated with three resolution phantoms in which the center-to-center distance of each rod was twice the rod diameter (Supplemental Fig. 7). First, a modified ultra-micro hot phantom (*22*) containing ^{22}Na gel (0.77 MBq) was scanned for 60 min at the center of the PET FOV. The modified ultra-micro hot phantom had six rod sectors (rod diameters of 0.75, 1.0, 1.35, 1.7, 2.0, and 2.4 mm) and axial length of 8 mm (Supplemental Fig. 7A). The number of coincidence events was about 22 million. For the image reconstruction, 10 iterations, 0.5 mm IDB kernel size and 440-560 keV energy window were used. The reconstructed transverse PET images were projected in the axial direction with the 8 mm thickness thereby producing an axially summed image. In addition, the effect of energy window on the spatial resolution was also investigated with various

energy windows of 250-750 keV to 350-650 keV, 400-600 keV, and 440-560 keV as ICS events can be discriminated based on pulse height information with the 3-layer DOI detector (*22,25*).

The same resolution phantom was also scanned by using a commercial preclinical PET scanner (Inveon D-PET; Siemens) (*8*) for 10 min with an energy window of 350-650 keV to obtain 24 million true coincidence events. The PET images were reconstructed by using two different algorithms of 2D FBP, and 2D OSEM, respectively. For the 2D OSEM, 16 subsets and 4 iterations were used. The voxel size of 0.194 × 0.194 × 0.796 mm^3, and matrix size of 256 × 256 × 159 were used for the Inveon PET image reconstruction.

Second, a SPECT rat phantom (*22*) having six different rod sectors (rod diameters of 0.7, 0.8, 0.9, 1.0, 1.2, and 1.5 mm) and 12 mm axial length was filled with ^{18}F of 2.1 MBq (Supplemental Fig. 7B). The SPECT rat phantom was placed at the center of the PET FOV and scanned for 60 min. The PET images were reconstructed using the OSEM with 10 iterations, 0.5 mm IDB kernel size and 440-560 keV energy window. Then the 48 slice images (12 mm axial thickness) were projected in the axial direction to generate a summed image.

Lastly, a PET mouse phantom having six rod sections (rod diameters of 0.45, 0.5, 0.55, 0.75, 0.8, 0.85 mm) and 10 mm axial length was filled with ^{18}F of 1.1 MBq (Supplemental Fig. 7C). The PET mouse phantom was placed at the center of the PET FOV, and then scanned for 60 min. For OSEM image reconstruction, 50 iterations and 440-560 keV energy window were used. The reconstructed transverse PET images were axially projected with a thickness of 10 mm (i.e. 40 slices) to generate a summed image.

For quantitative evaluation of the spatial resolution, the valley-to-peak ratio (VPR) was calculated from the line profiles of each rod sector. Subsequently, the resolvability (*22,27*) was calculated for each rod sector as follows:

$$\text{Resolvability} = \frac{N_{Rayleigh}}{N_{Total}} \times 100\%$$

where $N_{Rayleigh}$ is the number of line profiles with VPR below the Rayleigh criterion (i.e. VPR of 0.735 which corresponds to peak-to-valley ratio of 1.36) (*22,27*), and N_{Total} is the total number of line profiles for each rod sector. The effects of IDB kernel sizes on the SPECT rat and PET mouse phantom images were also investigated.

In vivo animal imaging

For metabotropic glutamate receptor imaging of a mouse brain, ^{18}F-FITM (*28*), a radioligand for metabotropic glutamate receptor 1, with a radioactivity dose of 7 MBq was administered to a 9-week-old, 20 g male nude BALB/cSlc-nu mouse via tail vein while the mouse was in the conscious state. The PET scan was performed for 30 min under the anesthesia condition with 1.5%-2.0% isoflurane 40 min after the injection. The iteration number of 20, IDB kernel size of 1.25 mm, and energy window of 440-560 keV were used for the 3D OSEM image reconstruction.

For glucose metabolism imaging of a mouse brain, ^{18}F-FDG with a radioactivity dose of 7 MBq was administered to a 7-week-old, 30.5-g male Slc:ddY mouse via tail vein while the mouse was in the conscious state. Then, the mouse was allowed to move freely inside a cage for 30 min without any anesthesia so as to induce metabolic trapping of the radiotracer, reflecting the cerebral glucose metabolism in an awake condition (*29*). Next, the mouse was

anesthetized using isoflurane to minimize motion artifacts during the PET scan, and a 30 min PET data acquisition was done 34 min after injection. Following this imaging session, an additional scan of the same mouse using the Inveon PET scanner was initiated 70 min after the radiotracer injection, and it lasted for 30 min. The Inveon PET data were reconstructed using 3D OSEM followed by maximum a posterior (MAP) with 16 subsets, 2 iterations and 350-650 keV energy window using the matrix size of 256 × 256 × 159. The numbers of prompt coincidence events were 20 million for the Inveon PET scanner and 24 million for the SR-PET scanner. After a series of two PET scans, the mouse underwent an x-ray computed tomography (CT) scan to obtain the anatomical information with a preclinical x-ray CT scanner (CosmoScan GX; Rigaku) using 70 kV tube voltage and 80 μA tube current. The x-ray CT images had the voxel size of 0.24×0.24×0.24 mm^3 and matrix size of 256×256×512. For the image co-registration between PET and x-ray CT images, the PMOD software (version 3.4) was used. For all mouse brain PET images, the central 25 mm × 25 mm square was cropped and displayed.

For glucose metabolism imaging of a rat brain, ^{18}F-FDG with a radioactivity dose of 12.3 MBq was administered to an 8-week-old, 283-g male Sprague Dawley rat via tail vein while the rat was in the conscious state. The rat brain was scanned for 50 min with the SR-PET under the anesthesia condition with isoflurane 140 min after the ^{18}F-FDG injection. The 10 iterations and 1.25 IDB kernel size, and energy window of 440-560 keV were used for the OSEM image reconstruction.

All the animal experiments were conducted in accordance with the animal experiment guidelines of the National Institutes for Quantum Science and Technology after being

approved by the local ethical committee of the institute.

RESULTS

Physical performance

The system coincidence timing resolution was 9.5 ns, and the system energy resolution was 24.3% (Fig. 2A). The axial sensitivity profiles had symmetric distributions with the peak axial sensitivities of 8.66%, 4.39%, 2.84%, and 1.56% for the energy windows of 250-750 keV, 350-650 keV, 400-600 keV, 440-560 keV, respectively (Fig. 2B). The peak NECR was decreased from 46.9 kcps to 5.14 kcps as the energy windows was narrowed down from 250-750 keV to 440-560 keV (Supplemental Fig. 8 and Supplemental Table. 2).

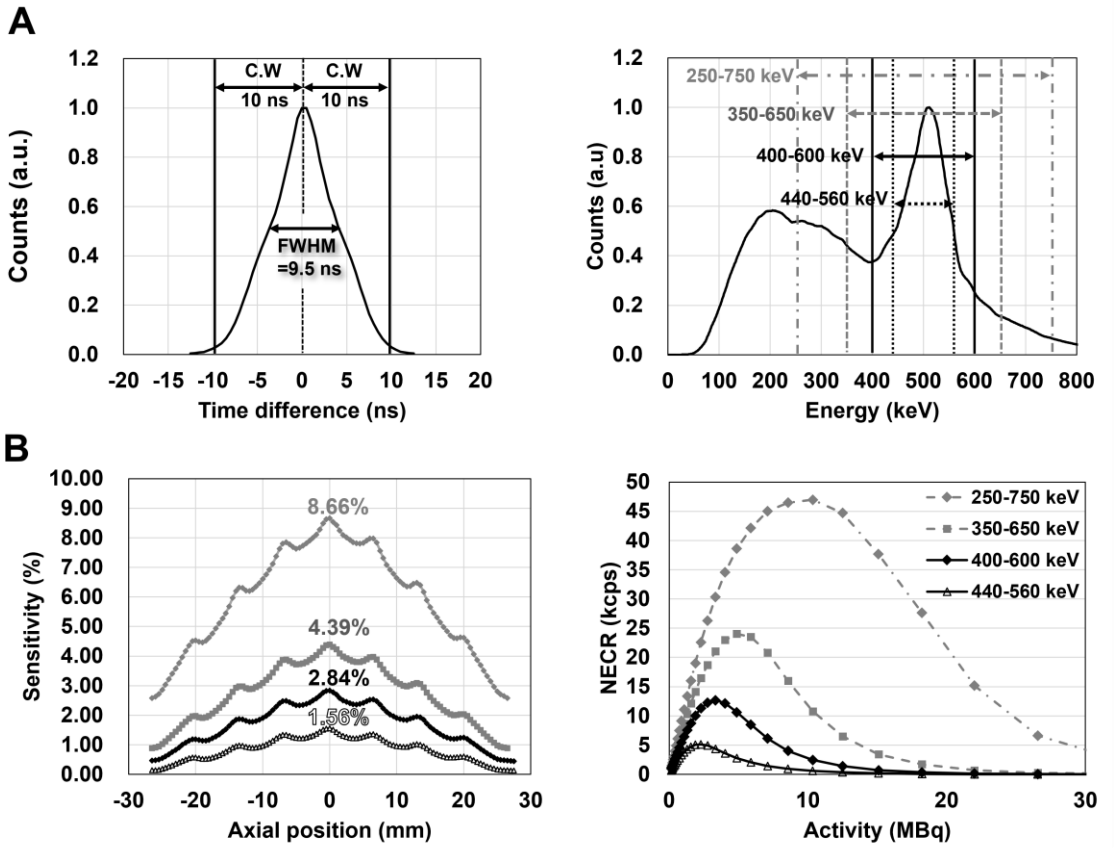

Fig. 2. (A) Global timing and energy spectra. (B) Axial sensitivity profiles, and NECR curves with different energy windows of 250-750, 350-650 keV, 400-600 keV, and 440-560 keV.

The average radial resolutions from center to the 10 mm radial offset position for the axial offset positions of center, 6.25 mm, 13.5 mm, and 19.75 mm were 1.00±0.16 mm, 0.91±0.05 mm, 0.98±0.12 mm, and 0.91±0.04 mm, with the FBP (Supplemental Table 3); and 0.61±0.19 mm, 0.58±0.19 mm, 0.56±0.19 mm, and 0.56±0.19 mm, with the OSEM (Supplemental Table 4).

The spatial resolution was dependent not only on the radial position but also axial position (Fig. 3). The axial resolution with the FBP was degraded at the axial offset of 0 mm and 13.5

mm where there were no direct LORs. The resolution degradations in axial and tangential directions were effectively reduced by using the OSEM algorithm which accounted for the geometrical factors. However, the axial resolution was degraded for the positions near the axial center due to the parallax error in axial direction. Even with high iterations over 10 (Supplemental Fig. 9), the radial resolution improvement for the radial offset of 10 mm and 15 mm was less dramatic compared to the radial offsets of within 5 mm due to the parallax error.

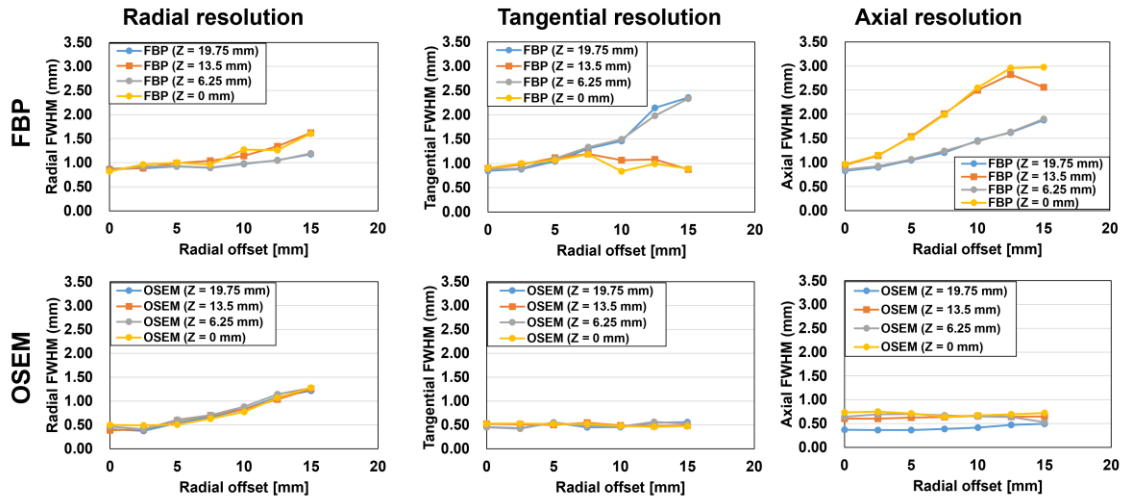

Fig. 3. The spatial resolution measurement results with the ^{22}Na point source at different radial and axial offset positions using an energy window of 440-560 keV. The radial, tangential and axial resolution with the FBP (top) and the OSEM using 10 iterations (Bottom).

The NEMA NU4 phantom images (Supplemental Fig. 10) and analysis results (Supplemental Table 5) indicate a good image quality in terms of recovery coefficient, uniformity, and spill over ratios.

Resolution phantom images

The 0.75 mm rod structures of the modified ultra-micro hot phantom were resolved with an average VPR of 0.543±0.065 and 100% resolvability (Fig. 4A). The 0.75 mm rod structure could also be resolved using the 2D FBP algorithm with an average VPR of 0.775±0.079 with a resolvability of 33.3% (Fig. 4B). In contrast, the Inveon PET could not resolve the 0.75 mm rod structure of the same phantom with FBP (Fig. 4C) and OSEM (Fig. 4D) due to the limited spatial resolution of 1.0-1.3 mm. For the SR-PET scanner, the spatial resolution was improved as the energy window was narrowed down from 250-750 keV to 440-560 keV (Supplemental Fig. 11 and 12) due the decreased ICS events at the expense of the sensitivity (Supplemental Table 6).

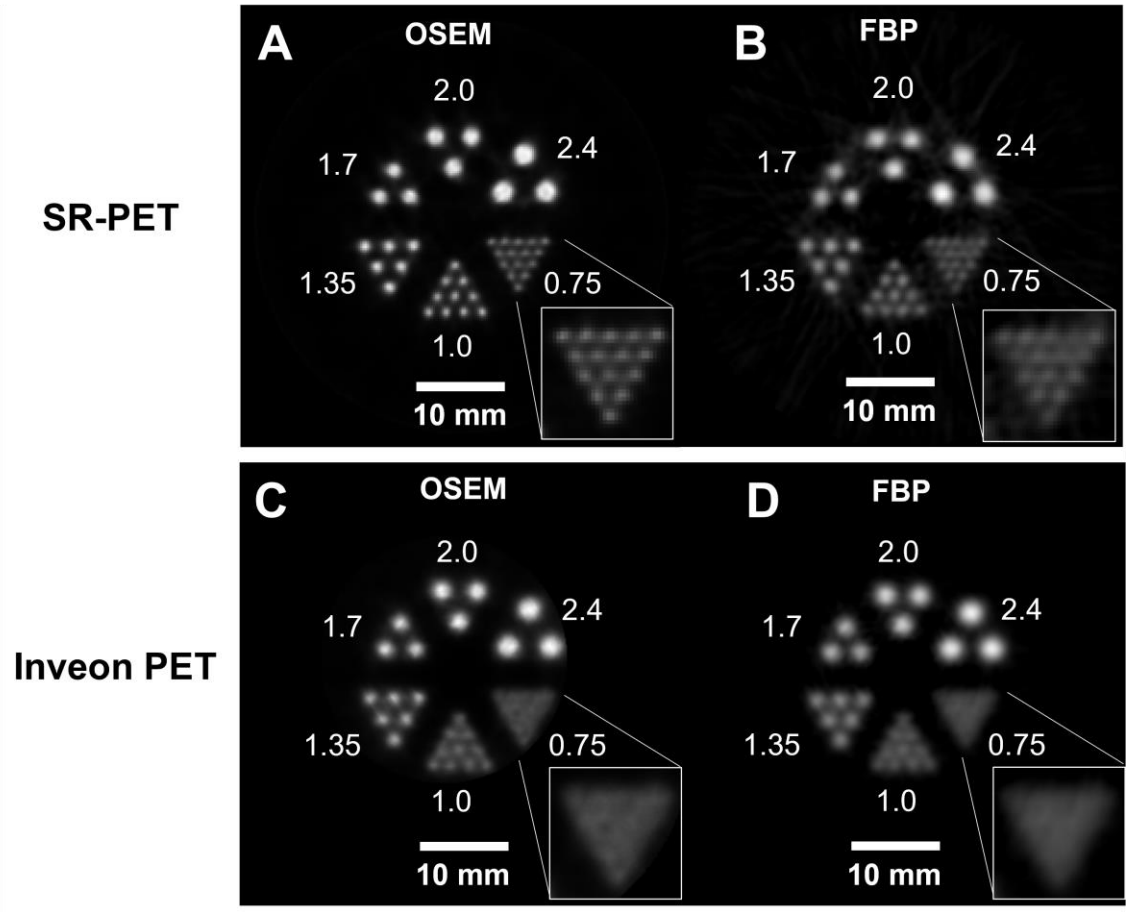

Fig. 4. The reconstructed PET images of the modified ultra-micro hot phantom with the SR-PET using the OSEM (A) and the FBP (B). The reconstructed PET images of the same phantom with the Inveon PET using the OSEM (C) and the FBP (D). The rod diameters are 0.75, 1.0, 1.35, 1.7, 2.0, and 2.0 mm. The inset represents the 0.75 mm rod sector.

For the reconstructed OSEM image of the SPECT rat phantom, all the rod patterns from 0.7 mm to 1.5 mm were resolved with 100% (Supplemental Table 7).

To resolve the sub-0.6 mm structures, 50 iterations were used for the PET mouse phantom (Supplemental Fig. 12), thereby resolving the 0.55 mm rod pattern with an average VPR of 0.527 (resolvability=100%) (Fig. 5). However, the resolvability for the 0.5 mm and 0.45 mm

rod patterns were only 55%, and 8%, respectively (Supplemental Table 7).

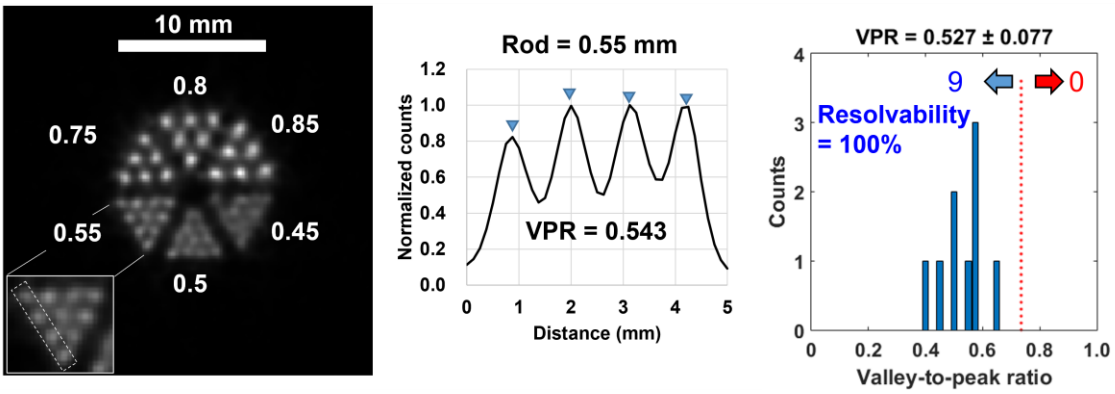

Fig. 5. The reconstructed PET image of the PET mouse phantom obtained with the SR-PET for 60 min after cropping the 25 mm × 25 mm central square (left). The line profiles of 0.55 mm rod sectors obtained as marked by the white dotted boxes of the insets (center). The VPR histogram for diameter of 0.55 mm (right). The numbers of line profiles with VPRs under and over 0.735 are shown at the left and right arrows, respectively.

In vivo rodent brain images

For rodent brain imaging, the IDB kernel size of 1.25 mm was used to smooth the images while keeping submillimeter resolution (Supplemental Fig. 14 and 15). Representative coronal mouse brain PET images at four different planes 1 mm apart were selected for visual display (Fig. 6). High accumulations of ^{18}F-FITM in the thalamus and cerebellum of the nude mouse could be observed in the PET images (Fig. 6A). The cortex, thalamus, hypothalamus, and amygdala of the nude mouse were also well delineated. In the sagittal image, the olfactory bulb and prefrontal cortex were well identified.

In the mouse brain images with ^{18}F-FDG, the cortex, thalamus, and hypothalamus which were closely located with only 0.5-0.75 mm separations could be identified (Fig. 6B). In

addition, the amygdala whose position was near the cortex could be identified also. In contrast to the SR-PET, the Inveon PET hardly resolved the brain structures of the same mouse due to the low spatial resolution (Fig. 6C).

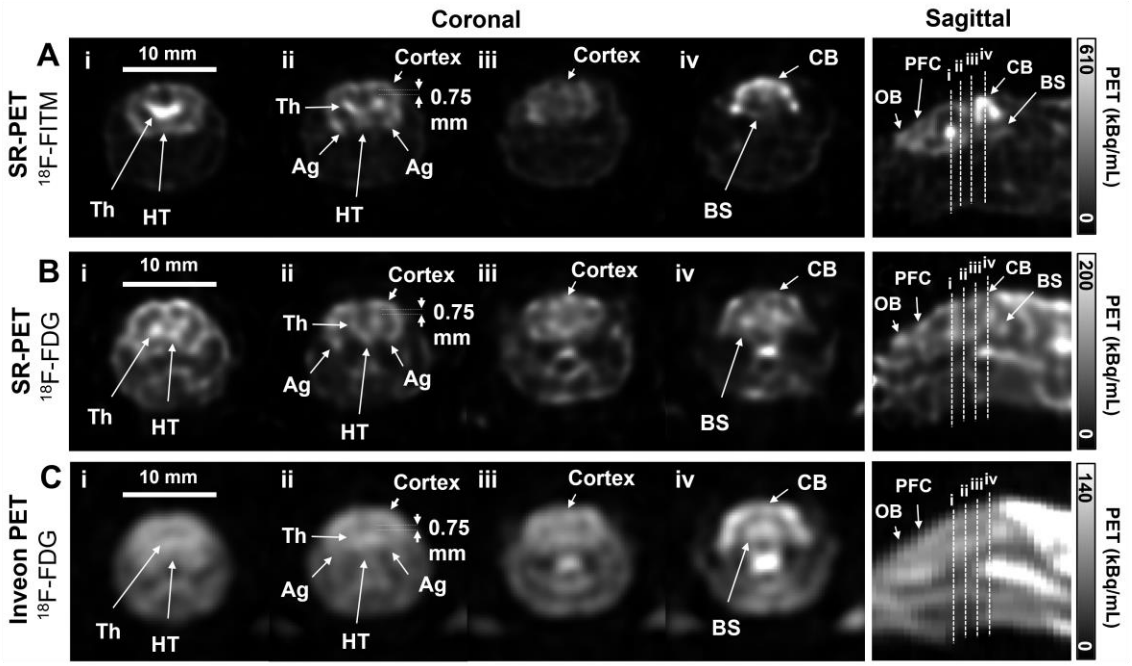

Fig. 6. (A) The mouse brain images of ^{18}F-FITM (7 MBq) obtained for 30 min with the SR-PET 40 min after injection. (B) The mouse brain images of ^{18}F-FDG (7 MBq) obtained for 30 min with the SR-PET 34 min after injection. (C) The mouse brain images of ^{18}F-FDG (7 MBq) obtained for 30 min with the Inveon D-PET 70 min after injection. For all images, the 25 mm × 25 mm central square was cropped and displayed. The coronal images were selected from the four different slices as indicated in the sagittal images by the white dotted vertical lines (i-iv). Ag = Amygdala; BS = Brain stem; CB = cerebellum. HT = Hypothalamus; OB = Olfactory bulb; Th = Thalamus; PFC = Prefrontal cortex.

The ^{18}F-FDG PET images of the mouse brain with SR-PET were well co-registered with the x-ray CT images in coronal, sagittal and transverse planes (Fig. 7). The detailed mouse brain structures were well delineated inside the cranial bone. In addition, the glucose

metabolism of the rat brain was also clearly visualized with the SR-PET (Supplemental Fig. 16).

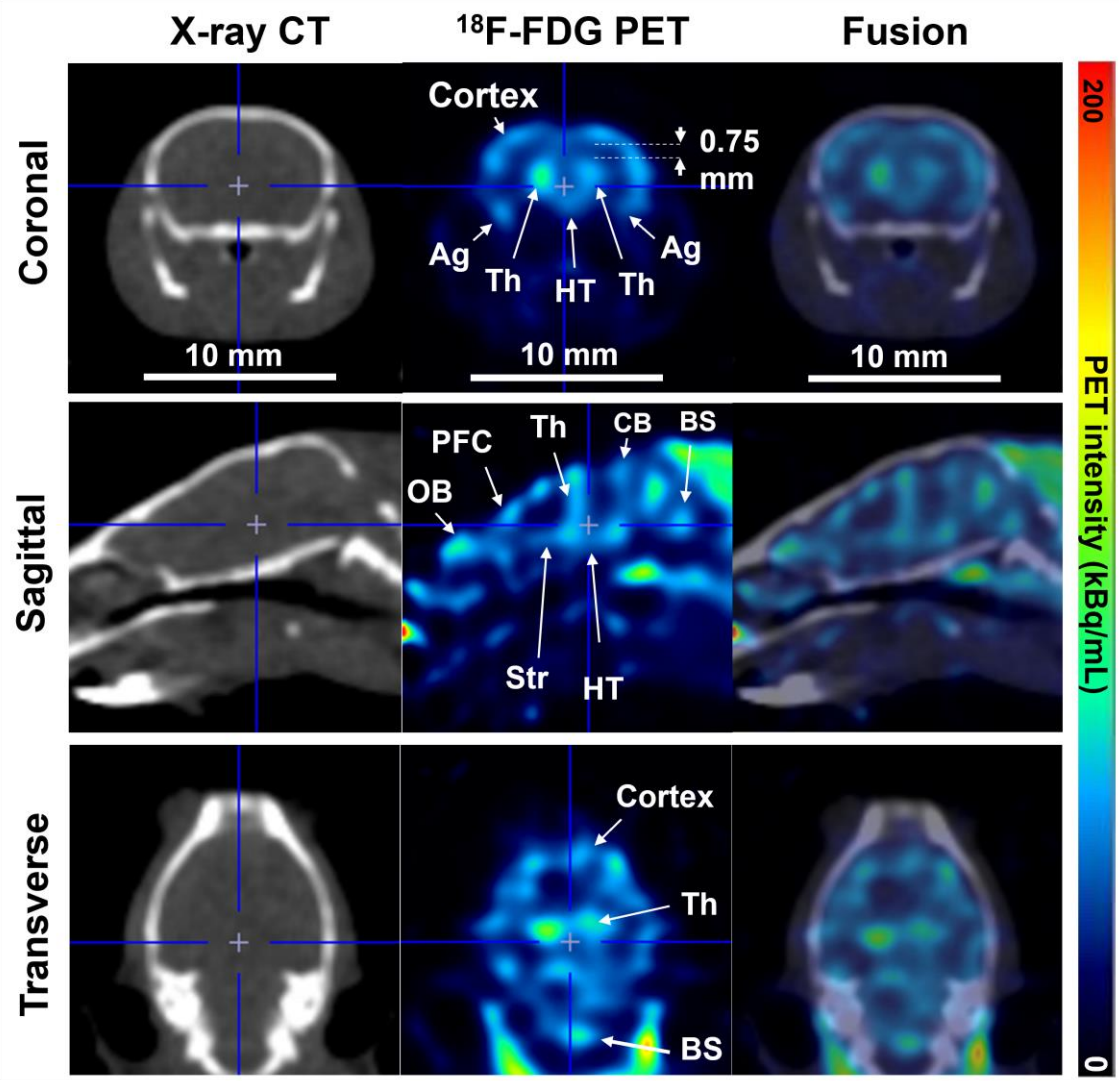

Fig. 7. Mouse brain images obtained with ^{18}F-FDG PET, x-ray CT, and their fusion in coronal (top), sagittal (middle), and transverse (bottom) planes. For all images, the 17 mm × 17 mm central square was cropped for image display. The white horizontal bar represents 10 mm. BS = Brain stem; CB = Cerebellum; HT = Hypothalamus; OB; Olfactory bulb; Str = Striatum; Th = Thalamus; PFC = Prefrontal cortex.

DISCUSSION

We developed the SR-PET using 3-layer DOI detectors that can achieve submillimeter spatial resolution in a 51.5 mm long axial coverage (Fig. 1). There are several factors that limit the spatial resolution of a small animal PET scanner (*20,30*), including: 1) crystal pitch; 2) crystal decoding error; 3) sampling error; 4) parallax error; 5) photon non-collinearity ; 6) positron range (*20*); and 7) ICS events (*21*). The fine crystal pitch (1 mm) combined with the staggered 3-layer DOI configuration can substantially minimize the sampling error (*31,32*) and parallax error (*30*). The staggered 3-layer DOI detector design allowed us to construct the PET scanner with small gaps between the detector blocks thereby minimizing the loss of projection information owing to detector gaps (*32*). The crystal decoding error (*30*) was substantially reduced by employing a diffusive reflector material ($BaSO_4$ powder) (*25*). The small ring diameter (52.5 mm) of the PET scanner minimized the spatial resolution degradation caused by the photon non-collinearity (*20*). Furthermore, the parallax error caused by the small ring diameter was effectively reduced by the 3-layer DOI information. Finally, the ICS events could be rejected with the narrow energy window of 440-560 keV (Supplemental Fig. 11 and 12) since ICS events have relatively lower or higher pulse height compared to photo-electric events due to the light collection efficiency difference that depends on the crystal layer (*22,25,33*). As a result, the SR-PET resolved the 0.55 mm rod structure with the resolvability of 100% (Fig. 5). Previously, the spatial resolution of 0.55 mm was reported by a research group at UC Davis (*34*). However, the axial FOV (7 mm) was too short to cover the entire brain of a mouse which is typically about 15 mm in length from the olfactory bulb to the cerebellum. The SPECT scanner employing a clustered pinhole

collimator dedicated to high energy radiations (e.g. 511 keV) has been shown to be able to resolve the 0.65 mm rod structure (*35*). However, the physical collimation technique demands an extremely high activity of over 20 MBq due to the poor sensitivity of 0.25%, whereas our small animal PET scanner provided the peak sensitivity of 1.56% even with the narrow energy window of 440-560 keV.

With the SR-PET, the closely located cortex, thalamus and hypothalamus were separately identified in the in vivo mouse brain images whereas the Inveon PET scanner could not distinguish the mouse brain structures whose ^{18}F-FDG distributions may have little changes due to washout (Fig. 6).

Although, the SR-PET resolved the 0.55 mm rods in the resolution phantom, the resolution for in vivo mouse brain imaging was degraded to around 0.85 mm due to the reduced iteration number (50 to 20) (Supplemental Fig. 13) and increased IDB kernel size (0.5 mm to 1.25 mm) (Supplemental Fig. 14). Thus, we plan to optimize the in vivo imaging protocol (e.g. injection does and scan time) to obtain more coincidence events so as to minimize the resolution loss especially by the IDB kernel size.

In addition, our next study will focus on integration of the PET scanner inside an ultrahigh-field MRI scanner to simultaneously obtain the high-resolution morphological information (*10,11,17,36*) while pushing the PET resolution limit further by using high magnetic field (*37,38*). Finally, we plan to use the SR-PET scanner to detect subtle changes in brain activity at the cortex region in Alzheimer disease mouse models (*39,40*).

CONCLUSION

We developed the SR-PET that can provide a spatial resolution approaching 0.55 mm in a 51.5 mm long axial coverage. The SR-PET can serve as a useful molecular imaging tool for translational neuroscience research using rodent models.

ACKNOWLEDGMENTS

This work was supported by Kakenhi grants (20H05667 and 21K19936), and grants from the Nakatani Foundation, the QST Future Laboratory Program, and the Directorate's Fund Project given by Dr. Takashi Nakano. We would also like to thank Dr. Tometeru Yamasaki, Dr. Atsushi B Tsuji, and Dr. Ming-Rong Zhang for their support in the small animal imaging experiments.

CONFLICTS OF INTEREST

No potential conflicts of interest relevant to this article exist.

KEY POINTS

QUESTION: Can we explore the mouse brain functions with submillimeter resolution in a high-sensitive small animal positron emission tomography scanner for neuroscience research?

PERTINENT FINDINGS: The developed SR-PET can provide a spatial resolution approaching 0.55 mm in a 51.5 mm long axial coverage. The glucose metabolism of a mouse brain can be visualized in detail by resolving the cortex, thalamus, hypothalamus, and amygdala which were barely distinguishable with a commercial preclinical PET scanner.

IMPLICATIONS FOR PATIENT CARE: The SR-PET can serve as a useful molecular imaging tool for translational neuroscience research and discovery of new drugs for neurodegenerative diseases in rodent models.

REFERENCES

1. Massoud TF, Gambhir SS. Molecular imaging in living subjects: seeing fundamental biological processes in a new light. *Genes Dev.* 2003;17:545-580.

2. Weissleder R, Pittet MJ. Imaging in the era of molecular oncology. *Nat.* 2008;452:580-589.

3. Misgeld T, Kerschensteiner M. In vivo imaging of the diseased nervous system. *Nat Rev Neurosci.* 2006;7:449-463.

4. Herfert K, Mannheim JG, Kuebler L, et al. Quantitative rodent brain receptor imaging. *Mol Imaging Biol.* 2020;22:223-244.

5. Phelps ME. PET: The merging of biology and imaging into molecular imaging. *J Nucl Med.* 2000;41:661-681.

6. Tai Y-C, Chatziioannou AF, Yang Y, et al. MicroPET II: design, development and initial performance of an improved microPET scanner for small-animal imaging. *Phys Med Biol.* 2003;48:1519-1537.

7. Tai Y-C, Ruangma A, Rowland D, et al. Performance Evaluation of the microPET Focus: A Third-Generation microPET Scanner Dedicated to Animal Imaging. *J Nucl Med.* 2005;46:455-463.

8. Bao Q, Newport D, Chen M, Stout DB, Chatziioannou AF. Performance evaluation of the inveon dedicated PET preclinical tomograph based on the NEMA NU-4 standards. *J Nucl Med.* 2009;50:401-408.

9. Goertzen AL, Bao Q, Bergeron M, et al. NEMA NU 4-2008 comparison of preclinical PET imaging systems. *J Nucl Med.* 2012;53:1300-1309.

10. Ko GB, Yoon HS, Kim KY, et al. Simultaneous multiparametric PET/MRI with silicon photomultiplier PET and ultra-high-field MRI for small-animal imaging. *J Nucl Med.* 2016;57:1309-1315.

11. Stortz G, Thiessen JD, Bishop D, et al. Performance of a PET insert for high-resolution small-animal PET/MRI at 7 Tesla. *J Nucl Med.* 2018;59:536-542.

12. Gaudin E, Thibaudeau C, Arpin L, et al. Performance evaluation of the mouse version of the LabPET II PET scanner. *Phys Med Biol.* 2021;66:065019.

13. Kuang Z, Wang X, Ren N, et al. Physical and imaging performance of SIAT aPET under different energy windows and timing windows. *Med Phys.* 2022;49:1432-1444.

14. Gu Z, Taschereau R, Vu NT, Prout DL, Lee J, Chatziioannou AF. Performance evaluation of HiPET, a high sensitivity and high resolution preclinical PET tomograph. *Phys Med Biol.* 2020;65:045009.

15. Vrigneaud JM, McGrath J, Courteau A, et al. Initial performance evaluation of a preclinical PET scanner available as a clip-on assembly in a sequential PET/MRI system. *Phys Med Biol.* 2018;63:125007.

16. Krishnamoorthy S, Blankemeyer E, Mollet P, Surti S, Van Holen R, Karp JS. Performance evaluation of the MOLECUBES β-CUBE—a high spatial resolution and high sensitivity small animal PET scanner utilizing monolithic LYSO scintillation detectors. *Phys Med Biol.* 2018;63:155013.

17. Gsell W, Molinos C, Correcher C, et al. Characterization of a preclinical PET insert in a 7 tesla MRI scanner: beyond NEMA testing. *Phys Med Biol.* 2020;65:245016.

18. Kim KY, Son JW, Kim K, et al. Performance Evaluation of SimPET-X, a PET Insert for Simultaneous Mouse Total-Body PET/MR Imaging. *Mol Imaging Biol.* 2021;23:703-713.

19. Miyaoka RS, Lehnert AL. Small animal PET: a review of what we have done and where we are going. *Phys Med Biol.* 2020;65:24TR04.

20. Levin CS, Hoffman EJ. Calculation of positron range and its effect on the fundamental limit of positron emission tomography system spatial resolution. *Phys Med Biol.* 1999;44:781-799.

21. Lee S, Lee JS. Inter-crystal scattering recovery of light-sharing PET detectors using convolutional neural networks. *Phys Med Biol.* 2021;66:185004.

22. Kang HG, Tashima H, Nishikido F, et al. Initial results of a mouse brain PET insert with a staggered 3-layer DOI detector. *Phys Med Biol.* 2021;66:215015.

23. Yoshida E, Tashima H, Shinaji T, et al. Development of a whole-body dual ring OpenPET for in-beam PET. *IEEE Trans Radiat Plasma Med Sci.* 2017;1:293-300.

24. Daube-Witherspoon ME, Muehllehner G. Treatment of axial data in three-dimensional PET. *J Nucl Med.* 1987;28:1717.

25. Kang HG, Nishikido F, Yamaya T. A staggered 3-layer DOI PET detector using BaSO4reflector for enhanced crystal identification and inter-crystal scattering event discrimination capability. *Biomed Phys Eng Express.* 2021;7:035018.

26. Gong K, Cherry SR, Qi J. On the assessment of spatial resolution of PET systems with iterative image reconstruction. *Phys Med Biol.* 2016;61:N193-202.

27. Hallen P, Schug D, Schulz V. Comments on the NEMA NU 4-2008 standard on performance measurement of small animal positron emission tomographs. *EJNMMI Phys.* 2020;7:12.

28. Yamasaki T, Fujinaga M, Kawamura K, et al. In vivo measurement of the affinity and density of metabotropic glutamate receptor subtype 1 in rat brain using 18F-FITM in small-animal PET. *J Nucl Med.* 2012;53:1601-1607.

29. Mizuma H, Shukuri M, Hayashi T, Watanabe Y, Onoe H. Establishment of in vivo brain imaging method in conscious mice. *J Nucl Med.* 2010;51:1068-1075.

30. Moses WW. Fundamental Limits of Spatial Resolution in PET. *Nucl Instrum Methods Phys Res A.* 2011;648 Supplement 1:S236-S240.

31. Derenzo SE, Budinger TF, Huesman RH, Cahoon JL, Vuletich T. Imaging properties of a positron tomograph with 280 BGO crystals. *IEEE Trans Nucl Sci.* 1981;28:81-89.

32. Zhang X, Stortz G, Sossi V, et al. Development and evaluation of a LOR-based image reconstruction with 3D system response modeling for a PET insert with dual-layer offset crystal design. *Phys Med Biol.* 2013;58:8379-8399.

33. Binder T, Kang HG, Nitta M, et al. Performance evaluation of a staggered three-layer DOI PET detector using a 1 mm LYSO pitch with PETsys TOFPET2 ASIC: comparison of HAMAMATSU and KETEK SiPMs. *Phys Med Biol.* 2021;66:125016.

34. Yang Y, Bec J, Zhou J, et al. A prototype high-resolution small-animal PET scanner dedicated to mouse brain imaging. *J Nucl Med.* 2016;57:1130-1135.

35. Goorden MC, Beekman FJ. High-resolution tomography of positron emitters with clustered pinhole SPECT. *Phys Med Biol.* 2010;55:1265-1277.

36. Judenhofer MS, Wehrl HF, Newport DF, et al. Simultaneous PET-MRI: a new approach for functional and morphological imaging. *Nat Med.* 2008;14:459-465.

37. Iida H, Kanno I, Miura S, Murakami M, Takahashi K, Uemura K. A simulation study of a method to reduce positron annihilation spread distributions using a strong magnetic field in positron emission tomography. *IEEE Trans Nucl Sci.* 1986;33:597-600.

38. Christensen NL, Hammer BE, Heil BG, Fetterly K. Positron emission tomography within a magnetic field using photomultiplier tubes and lightguides. *Phys Med Biol.* 1995;40:691-697.

39. Deleye S, Waldron AM, Verhaeghe J, et al. Evaluation of small-snimal PET outcome measures to detect disease modification induced by BACE inhibition in a transgenic mouse model of Alzheimer disease. *J Nucl Med.* 2017;58:1977-1983.

40. Kimura T, Ono M, Seki C, et al. A quantitative in vivo imaging platform for tracking pathological tau depositions and resultant neuronal death in a mouse model. *Eur J Nucl Med Mol Imaging.* 2022;In press.

Graphical Abstract

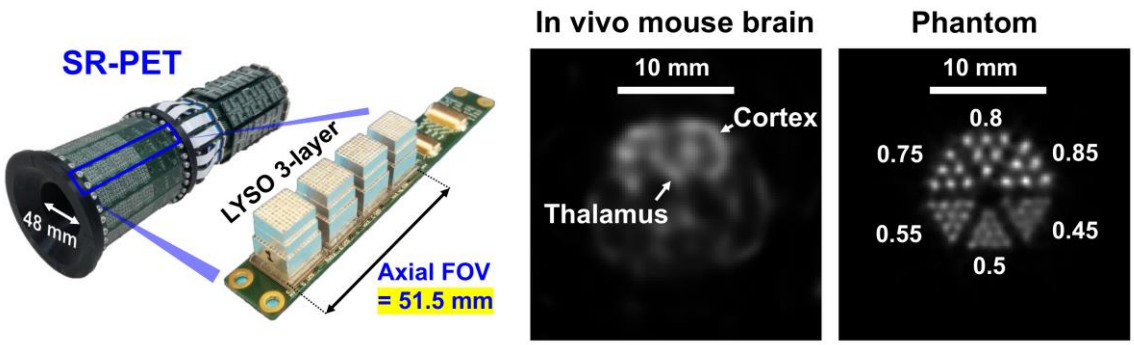

Supplemental Data

Submillimeter resolution positron emission tomography for high-sensitivity mouse brain imaging

Han Gyu Kang[1], Hideaki Tashima[1], Hidekatsu Wakizaka[1], Fumihiko Nishikido[1], Makoto Higuchi[2], Miwako Takahashi[1], Taiga Yamaya[1]

[1]Department of Advanced Nuclear Science, National Institutes for Quantum Science and Technology (QST), 4-9-1, Anagawa, Inage-ku, Chiba, Japan

[2]Department of Functional Brain Imaging, National Institutes for Quantum Science and Technology (QST), 4-9-1, Anagawa, Inage-ku, Chiba, Japan

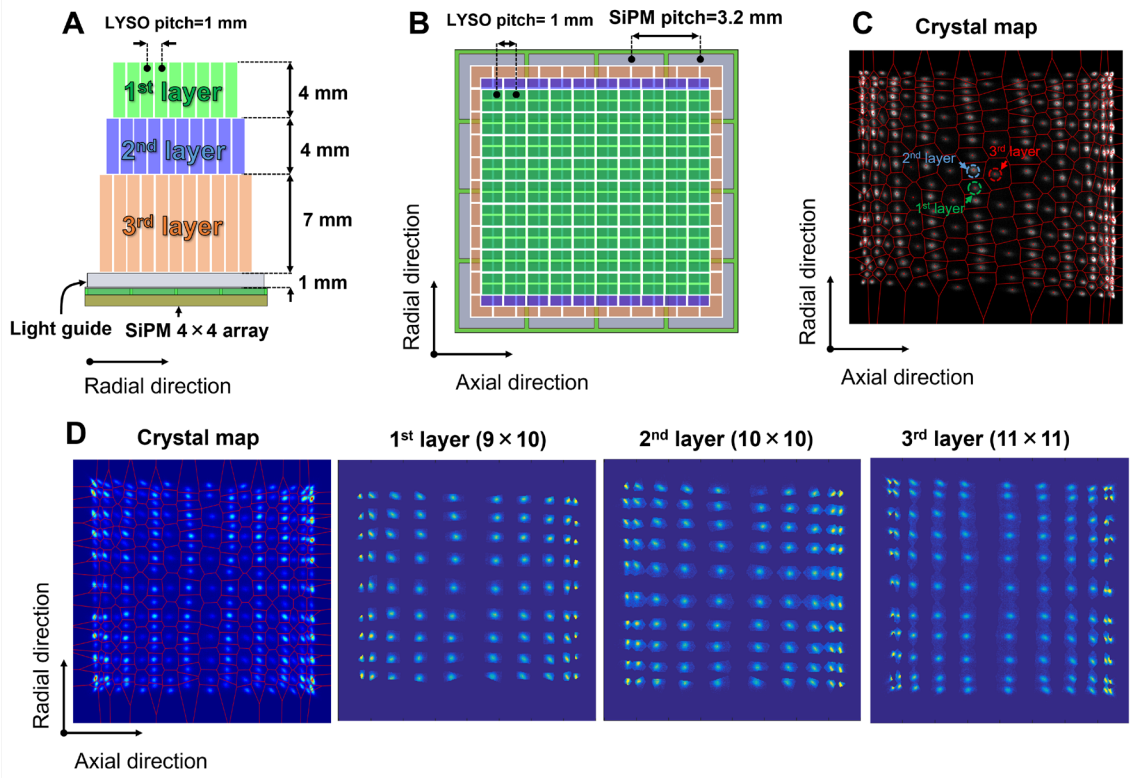

SUPLEMENTAL FIGURE 1. (A) Front view of a staggered 3-layer DOI detector consisting of LYSO crystal array, a light guide, and SiPM 4×4 array. The 1st, 2nd, and 3rd layers had a relative offset of a crystal half pitch to each other in the radial direction. (B) Top view of the staggered 3-layer DOI detector. (C) The crystal map response of a DOI detector with the Voronoi diagram. The 1st, 2nd, and 3rd layers are marked by green, blue, and red circles, respectively. The crystal positions are marked by red dots. (D) The crystal maps of the 1st, 2nd, and 3rd layers after segmentation using the Voronoi diagram.

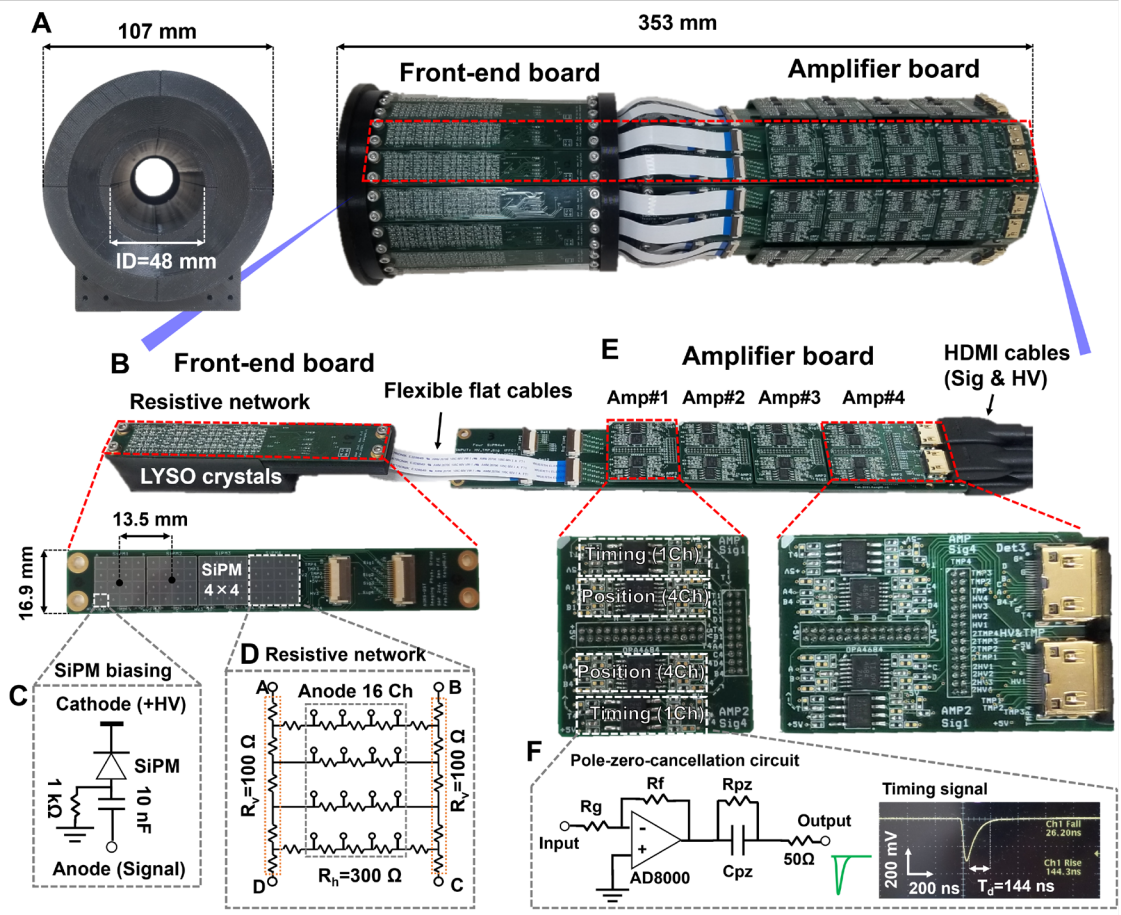

SUPPLEMENTAL FIGURE 2. (A) The front view and side view of the developed ultrahigh resolution small animal PET scanner (hereafter referred to SR-PET). (B) Front-end board consisting of four 4×4 SiPM arrays. (C) SiPM biasing to the cathode and signal extraction from the anode with the decoupling capacitor and shunt resistor. (D) A resistive network for position decoding (R_h = 300 Ω, R_v = 100 Ω). (E) One of the amplifier boards that consisted of four add-on amplifier boards. (F) Pole-zero-cancellation circuit used for timing signal. The pole-zero-cancellation circuit (C_{pz} = 100 pF, R_{pz} = 1 kΩ) was implemented into the output terminal of the timing channel. The assembling procedure of the SR-PET scanner was recorded as a time-lapse video (Supplemental Video 1). C_{pz} = pole-zero capacitor; T_d = decay time; R_h = horizontal resistor; R_v = vertical resistor; R_g = gain resistor; R_f = feedback resistor; R_{pz} = pole-zero resistor; Sig = signal.

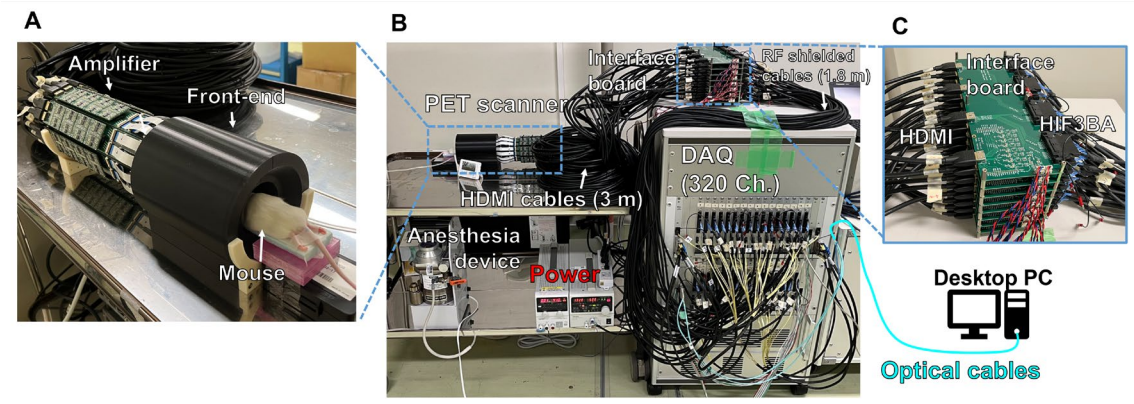

SUPPLEMENTAL FIGURE 3. (A) The SR-PET scanner with a mouse. A black light-tight cylindrical cover was used only for the front-end part to block the external light from the SiPM arrays. (B) The entire SR-PET system with the interface board and DAQ. The SiPM signals were transferred from the PET scanner to the interface board via 3 m long high-definition multimedia interface cables. The SiPM signals were transferred from the interface board to the DAQ system via 1.8 m long RF shielded cables. Two optical cables were used to transmit and receive the digitized signals between the DAQ and PC. (C) Eight interface boards were used to convert the high-definition multimedia interface cables type-A to the HIF3BA-26PA-2.54DS connector before feeding the SiPM analog signals to the DAQ system. HDMI:

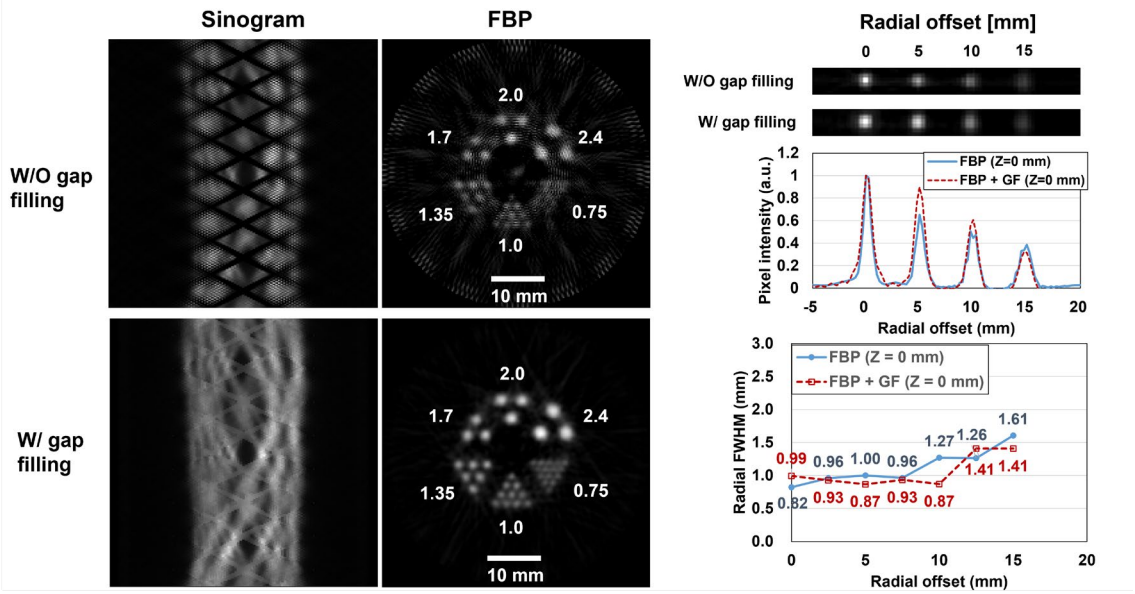

SUPPLEMENTAL FIGURE 4. The effects of gap filling (GF) on the sinograms and reconstructed FBP images of the modified ^{22}Na ultra-micro hot phantom for energy window of 440-560 keV (left). The sinogram and the FBP images were generated after summing 32 slices (8 mm thickness). The gap filling with a linear interpolation method effectively reduced the artifact across of the FOV. Especially the artifact at the center of the FOV was removed with the gap filling. The ^{22}Na point source images at the axial center, line profiles and corresponding radial FWHM without and with the gap filling (right). The gap filling method did not degrade the spatial resolution except at the center of the FOV.

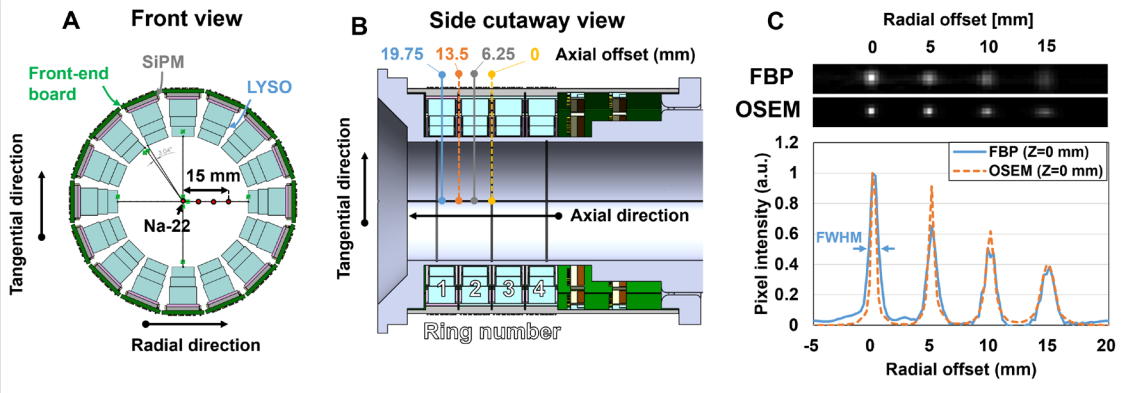

SUPPLEMENTAL FIGURE 5. (A) Front view of the SR-PET scanner with different radial ^{22}Na source positions from the center to 15 mm with 2.5 mm spacing. (B) Side cutaway view of the SR-PET scanner. The spatial resolutions in radial, tangential, and axial directions were obtained at different axial offset positions of center, 6.25 mm, 13.5 mm, and 19.75 mm using the FBP and OSEM algorithms. (C) The reconstructed PET images with the FBP and OSEM at the axial center and their corresponding line profiles.

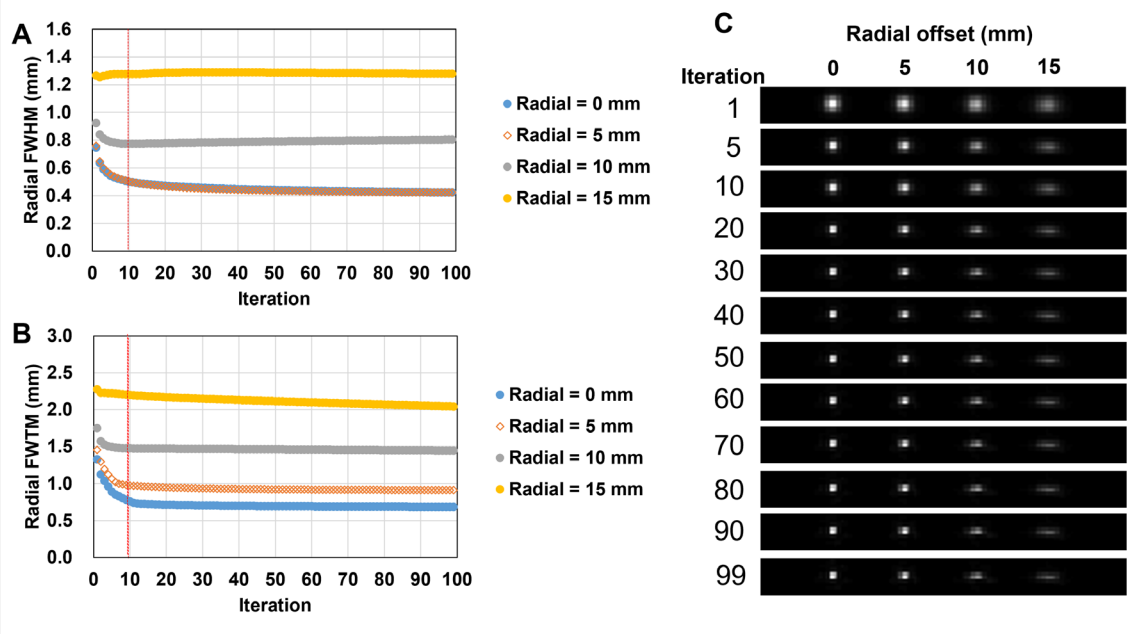

SUPPLEMENTAL FIGURE 6. The spatial resolution measurement results with the ^{22}Na point source at axial center as a function of iteration. (A) Spatial resolution in FWHM and (B) FWTM. The resolution results at radial offset positions of 0 mm, 5 mm, 10 mm, and 15 mm are represented by the blue circle, orange empty diamond, grey box, and yellow triangle, respectively. The 10 iteration is marked by the red vertical line. (C) The reconstructed OSEM PET images with different iterations for different radial offsets at the axial center.

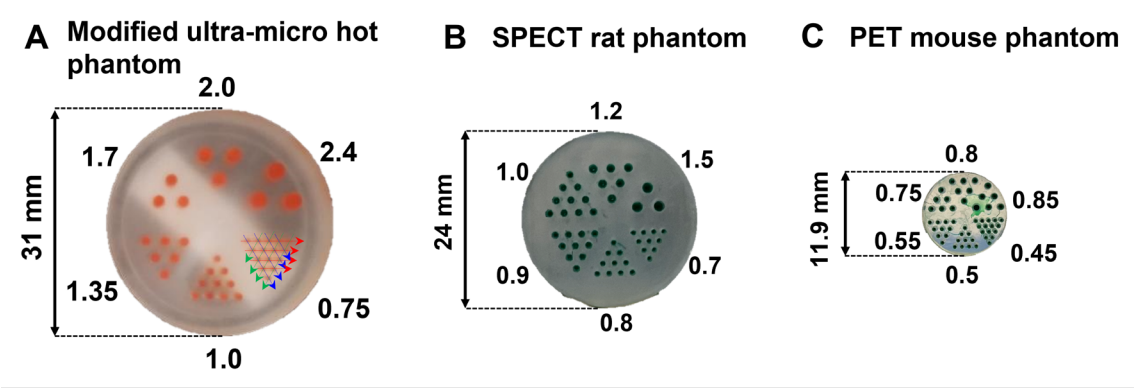

SUPPLEMENTAL FIGURE 7. (A) The modified ultra-micro hot phantom containing ^{22}Na gel. The rod diameters were 0.75, 1.0, 1.35, 1.7, 2.0, and 2.0 mm for each sector. The line profiles in three different directions were obtained as indicated by red, blue, and green color arrows to calculate the resolvability. (B) The SPECT rat phantom filled with ^{18}F source. The rod diameters were 0.7, 0.8, 0.9, 1.0, 1.2, and 1.5 mm. (C) The PET mouse phantom filled with ^{18}F source. The rod diameters were 0.45, 0.5, 0.55, 0.75, 0.8, and 0.85 mm.

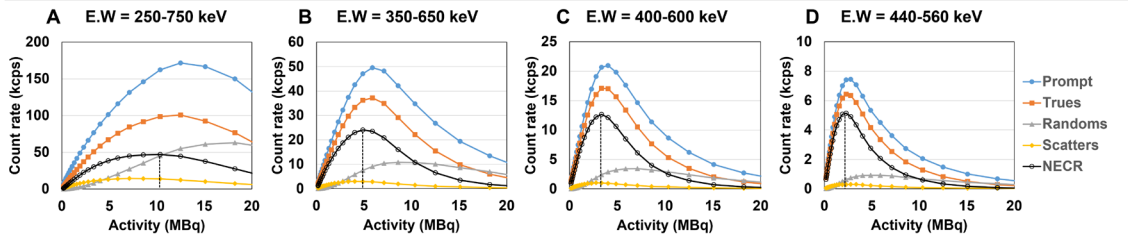

SUPPLEMENTAL FIGURE 8. The count rate performance obtained using the mouse-like phantom with different energy windows of (A) 250-750 keV, (B) 350-650 keV, (C) 400-600 keV, and (D) 440-560 keV. The peak NECR of each energy window is indicated by a vertical dotted line.

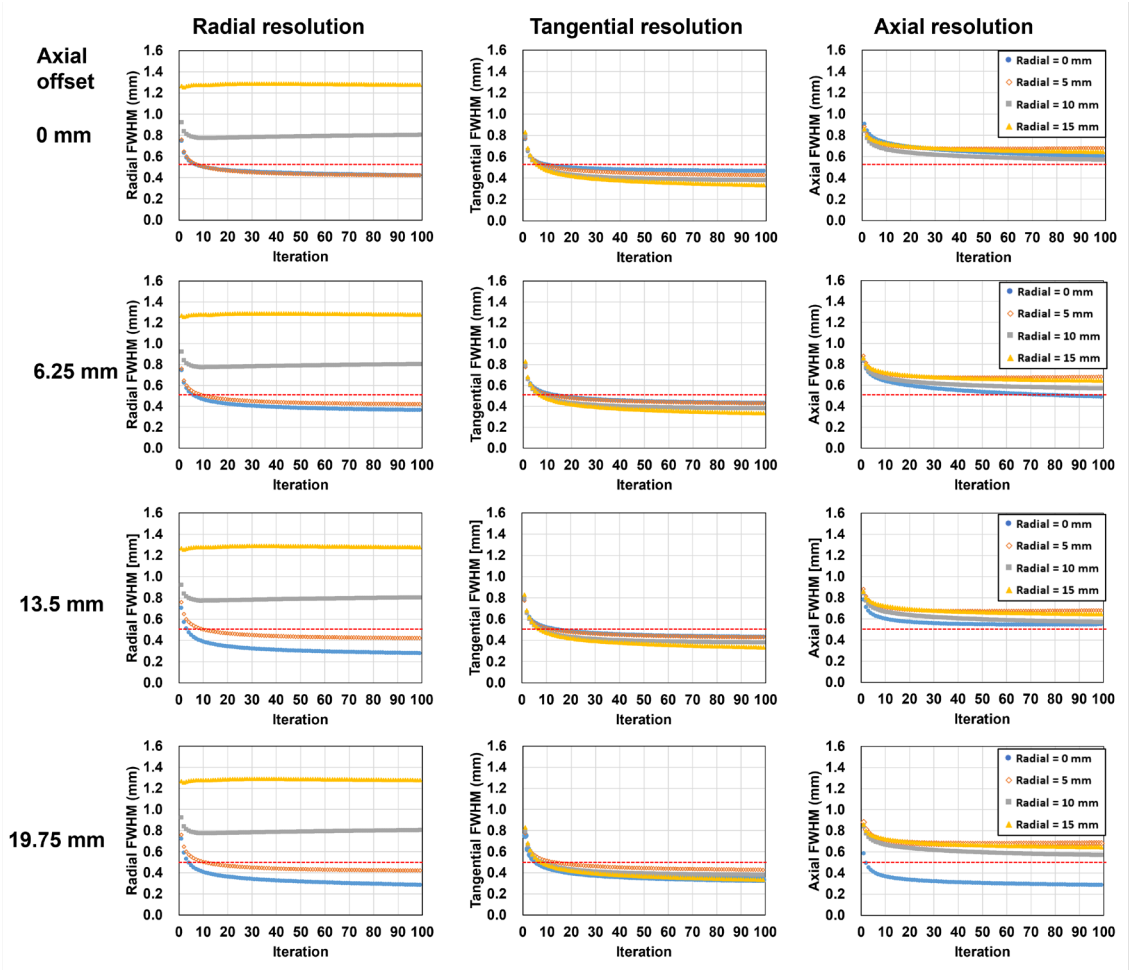

SUPPLEMENTAL FIGURE 9. The spatial resolution measurement results in FWHM with the ^{22}Na point source as a function of iteration. The FWHM at radial offset positions of 0 mm, 5 mm, 10 mm, and 15 mm are represented by the blue circle, orange empty diamond, grey box, and yellow triangle, respectively. The 0.5 mm FWHM is marked by the red broken horizontal line.

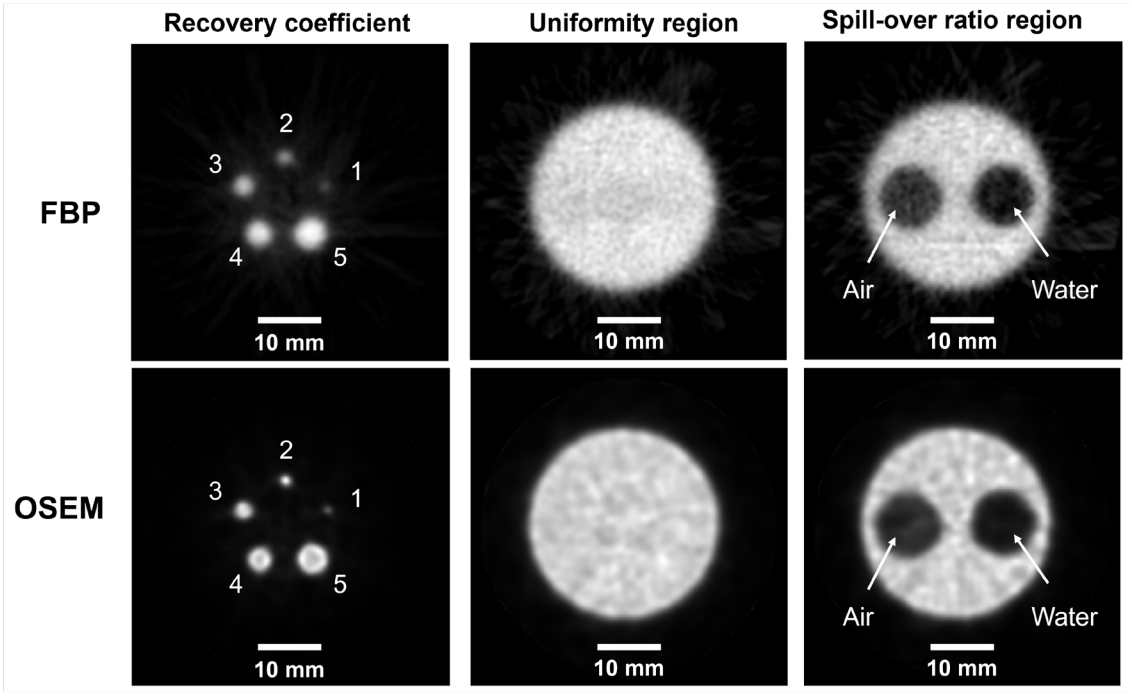

SUPPLEMENTAL FIGURE 10. The reconstructed PET images of the NEMA NU4 image quality phantom with the FBP (top) and the OSEM (bottom) for the recovery coefficient (left), uniformity (center), and spill-over-ratio (right) regions. The rod diameters for the recovery coefficient region were 1, 2, 3, 4, and 5 mm, respectively. The energy window of 400-600 keV was used. For the FBP, the gap filling method was used without applying any post processing filter. For the OSEM, IDB kernel size of 1.25 mm was used with 10 iterations. The axially projected slice thickness for the recovery coefficient, uniformity, and spill-of-ratio regions were, the 16 mm, 11 mm, and 14 mm, respectively.

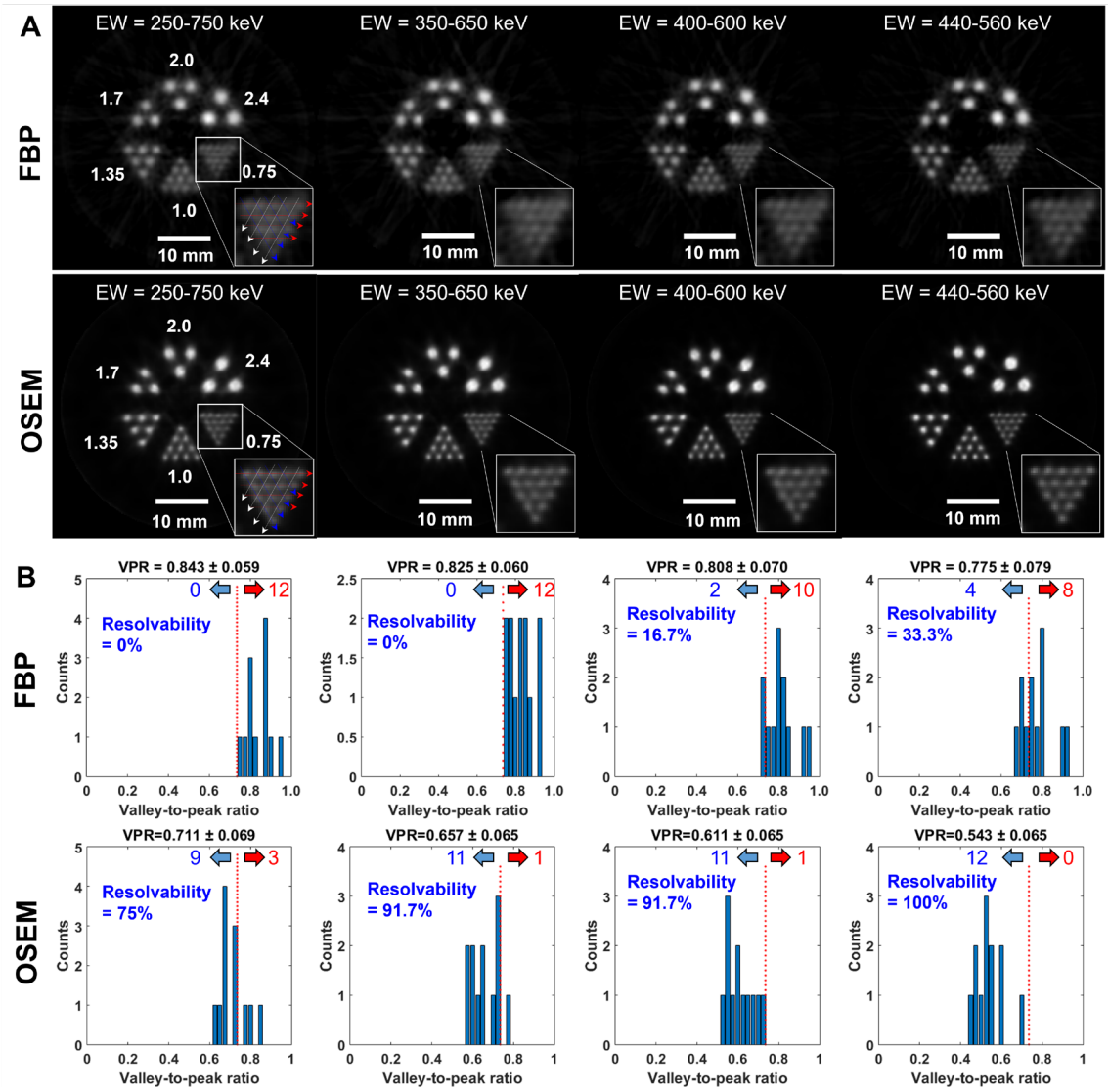

SUPPLEMENTAL FIGURE 11. (A) The reconstructed PET images of the modified ultra-micro hot phantom (^{22}Na of 0.7 MBq) using FBP (top) and the OSEM (bottom) with different energy windows of 250-750 keV, 350-650 keV, 400-600 keV, and 440-560 keV. The rod diameters are 0.75, 1.0, 1.35, 1.7, 2.0, and 2.4 mm in the clockwise direction. The line profiles were obtained for the 0.75 mm rod structure as indicated by the arrows in the inset. (B) The histogram of VPRs for the 0.75 mm rod structure obtained with the different energy windows using the FBP and OSEM algorithms. The Rayleigh criterion of 0.735 is indicated by a vertical dotted red line. The numbers of line profiles under and over the Rayleigh criterion are indicated at the left and right arrows, respectively.

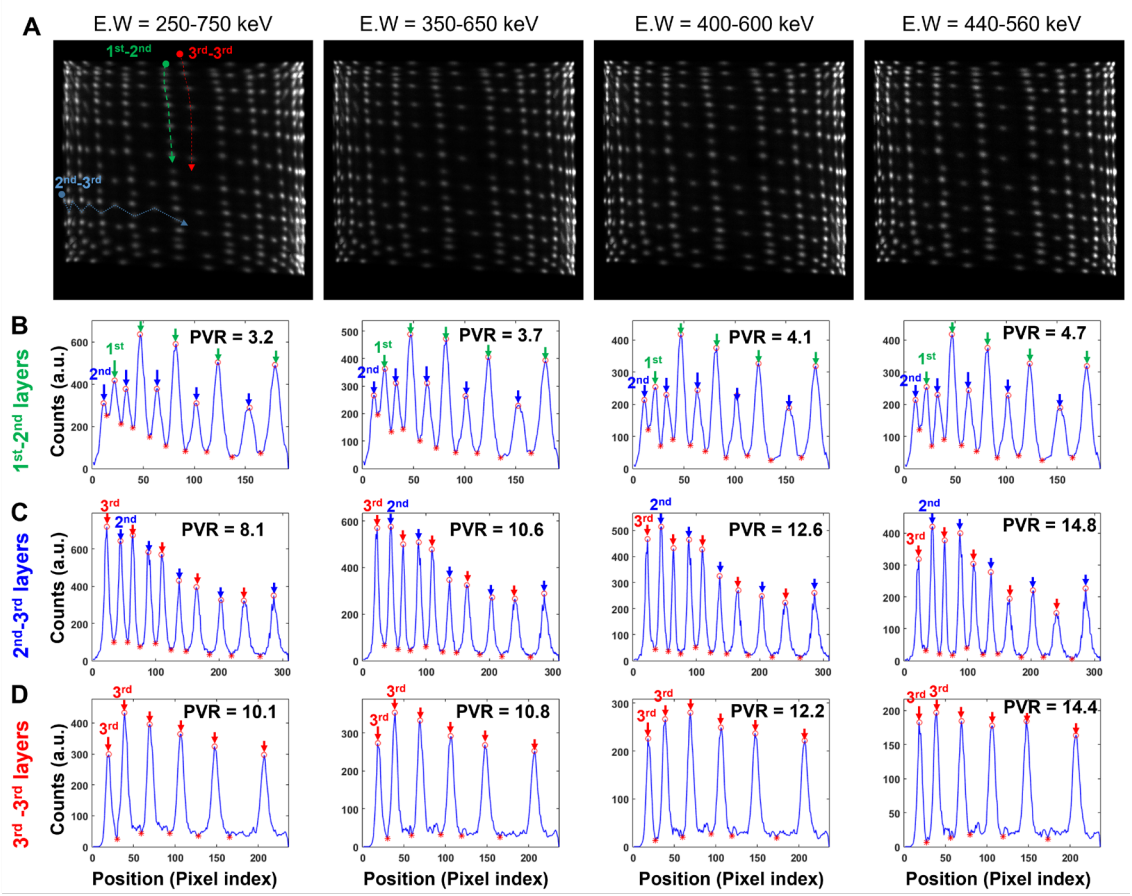

SUPPLEMENTAL FIGURE 12. (A) The crystal map of a DOI detector with different energy windows of 250-750 keV, 350-650 keV, 400-600 keV, and 440-560 keV. The line profiles were extracted from the edge to the center direction as indicated by the green (1^{st}-2^{nd} layers), blue (2^{nd}-3^{rd} layers), and red (3^{rd}-3^{rd} layers) arrows. (B) The line profiles along the 1^{st}-2^{nd} layers. The peak positions of the 1^{st} and 2^{nd} layers are marked by green and blue arrows, respectively. (C) The line profiles along the 2^{nd}-3^{rd} layers. The peak positions of the 2^{nd} and 3^{rd} layers are marked blue and red arrows, respectively. (D) The line profiles along the 3^{rd} layer. The peak positions of 3^{rd} layer are marked by red arrows. The average peak-to-valley ratio (PVR) was increased about 1.4 times as the energy window was narrowed down from 250-750 keV to 440-560 keV mainly due to the rejection of the inter-crystal scattering events.

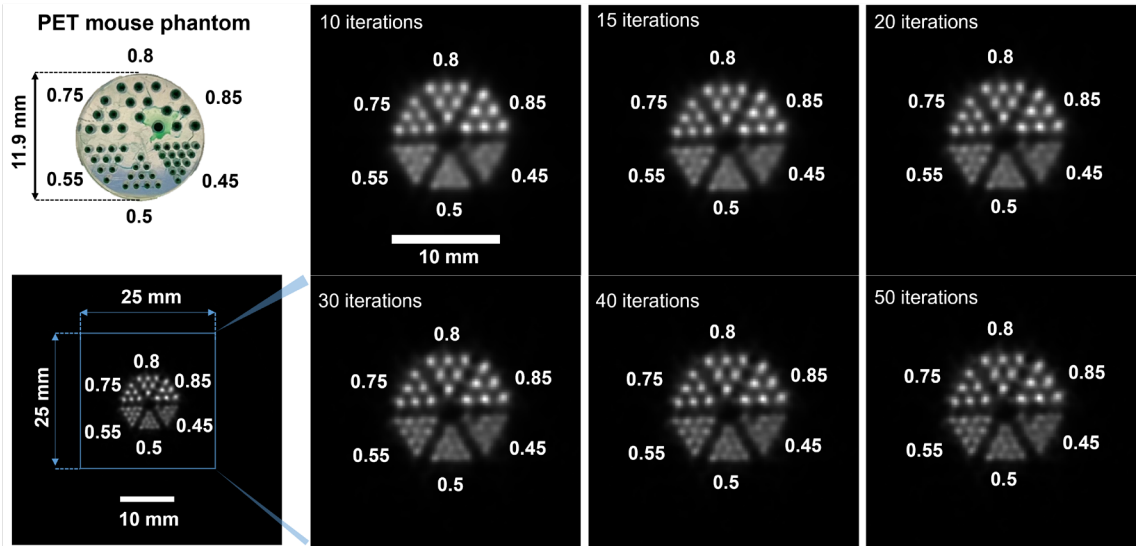

SUPPLEMENTAL FIGURE 13. The reconstructed PET images of the PET mouse phantom obtained using different iterations of 10, 15, 20, 30, 40, and 50. The PET mouse phantom had rods of six different diameters: 0.45, 0.5, 0.75, 0.8 and 0.85 mm. The energy window of 440-560 keV and IDB kernel size of 0.5 mm were used. The central 25 mm × 25 mm square was cropped for the image display.

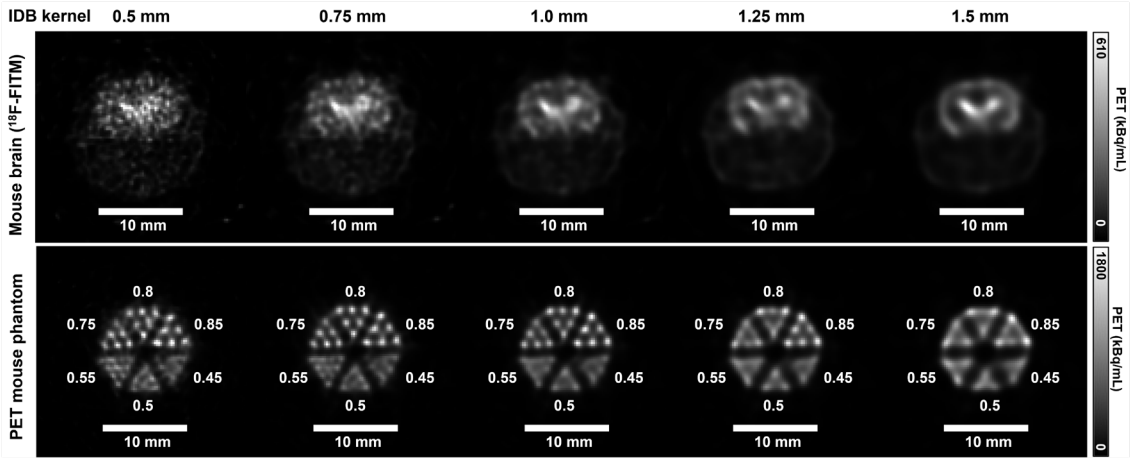

SUPPLEMENTAL FIGURE 14. The reconstructed OSEM PET images of a single selected slice with different image domain blurring (IDB) kernel sizes (0.5, 0.75, 1.0, 1.25, and 1.5 mm). (Top) The mouse brain images of ^{18}F-FITM (injection dose = 7 MBq) obtained for 30 min with a post injection time of 40 min. (Bottom) The PET mouse phantom images were obtained for 60 min. The phantom was filled with the ^{18}F of 2.1 MBq. The number of iterations and subsets were 20 and 8, respectively. The central 25 mm × 25 mm square was cropped for the image display.

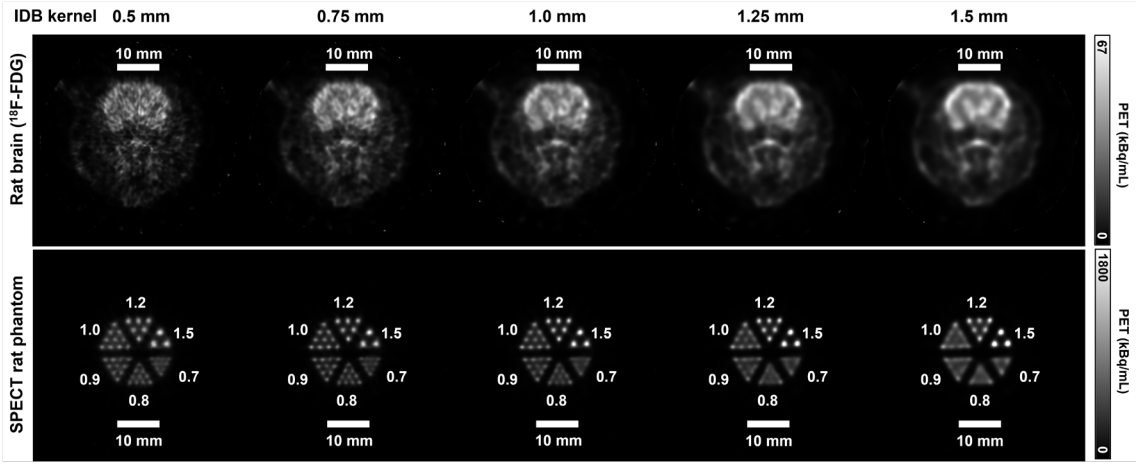

SUPPLEMENTAL FIGURE 15. The reconstructed OSEM PET images of a single selected slice with different image domain blurring (IDB) kernel sizes (0.5, 0.75, 1.0, 1.25, and 1.5 mm). (Top) The in vivo glucose metabolism images of a rat brain obtained for 50 min. The injection dose of ^{18}F-FDG was 12.3 MBq, and the post injection time was 140 min. (Bottom) The SPECT rat phantom images obtained for 60 min. The phantom was filled with ^{18}F of 2.1 MBq. The number of iterations and subsets were 10 and 8, respectively. The energy window of 440-560 keV was used.

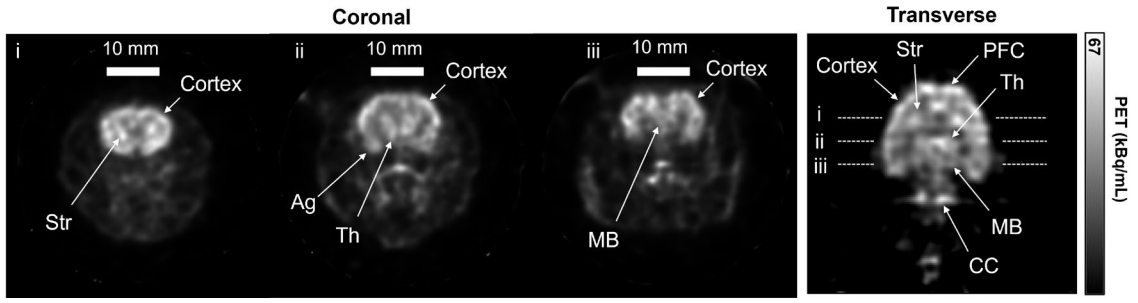

SUPPLEMENTAL FIGURE 16. The reconstructed rat brain images with OSEM algorithm using 10 iterations, IDB kernel size of 1.25 mm and energy window of 440-560 keV. The coronal images were selected from the three different slices as indicated in the transverse image by the white dotted horizontal lines (i-iii). The cortex, amygdala, striatum, thalamus and midbrain were identified. Ag = Amygdala; BS = Brain stem; CC = Colliculus; MB: midbrain; Th = Thalamus; PFC = Prefrontal cortex.

SUPPLEMENTAL TABLE 1. The Iterative Image Reconstruction Parameters for Various Imaging Objects.

Imaging object	Iteration	Subset	IDB kernel size	Energy window
NEMA ^{22}Na point source	10	8	0.5 mm	440-560 keV
NEMA NU4 phantom	10	8	1.25 mm	400-600 keV
Modified ultra-micro hot phantom	10	8	0.5 mm	440-560 keV
SPECT rat phantom	10	8	0.5 mm	440-560 keV
PET mouse phantom	50	8	0.5 mm	440-560 keV
Mouse brain	20	8	1.25 mm	440-560 keV
Rat brain	10	8	1.25 mm	440-560 keV

SUPPLEMENTAL TABLE 2. The Count Rate Performance with the Mouse-Like Phantom.

Energy window [keV]	Peak NECR [kcps]	Activity [MBq][a]	NECR at 3.7 MBq	Scatter fraction [%][b]	Random fraction [%][c]
250-750	46.9	10.35	34.5	15.3	28.0
350-650	24.0	4.87	18.7	11.1	15.8
400-600	12.7	3.34	12.1	8.1	11.6
440-560	5.14	2.29	4.4	4.0	8.5

[a]The activity at which the peak NECR was obtained.

[b]The scatter fraction was obtained at the activity for which the random fraction was below 1.0%

[c]The random fraction was obtained at the activity of the peak NECR.

SUPPLEMENTAL TABLE 3. The Spatial Resolutions at the Various Axial and Radial Off set Positions With FBP. The FWTM Results are Given in the Parentheses.

Axial offset [mm]	Radial offset [mm]	0	5	10	15
0	Radial	0.82 (1.56)	1.00 (2.13)	1.27 (2.73)	1.61 (3.10)
0	Tangential	0.90 (1.77)	1.07 (1.84)	0.84 (1.45)	0.89 (1.48)
0	Axial	0.96 (1.82)	1.52 (2.63)	2.55 (4.13)	2.97 (5.61)
0	Volumetric	0.72 (5.03)	1.63 (10.30)	2.72 (16.33)	4.25 (25.72)
6.25	Radial	0.84 (1.63)	0.94 (1.68)	0.98 (1.71)	1.20 (2.11)
6.25	Tangential	0.87 (1.73)	1.10 (2.13)	1.50 (4.53)	2.33 (6.73)
6.25	Axial	0.85 (1.58)	1.06 (1.87)	1.44 (2.60)	1.90 (3.46)
6.25	Volumetric	0.62 (4.42)	1.08 (6.66)	2.11 (20.11)	5.31 (49.14)
13.5	Radial	0.86 (1.75)	0.99 (1.75)	1.14 (2.30)	1.62 (3.34)
13.5	Tangential	0.90 (1.61)	1.11 (2.31)	1.06 (1.65)	0.87 (1.38)
13.5	Axial	0.95 (1.75)	1.54 (2.70)	2.50 (4.08)	2.56 (5.42)
13.5	Volumetric	0.73 (4.94)	1.70 (10.88)	3.03 (15.41)	3.63 (24.93)
19.75	Radial	0.88 (1.63)	0.92 (1.71)	0.97 (1.60)	1.18 (2.08)
19.75	Tangential	0.85 (1.53)	1.04 (1.96)	1.46 (4.33)	2.35 (8.10)
19.75	Axial	0.83 (1.53)	1.05 (1.93)	1.45 (2.67)	1.88 (3.43)
19.75	Volumetric	0.62 (3.81)	1.01 (6.44)	2.06 (18.59)	5.20 (57.77)

SUPPLEMENTAL TABLE 4. The Spatial Resolutions at the Various Axial and Radial Off set Positions With OSEM. The FWTM Results are Given in the Parentheses. The number of iterations was 10 and IDB kernel size was 0.5 mm.

Axial offset [mm]	Radial offset [mm]	0	5	10	15
0	Radial	0.50 (0.76)	0.50 (0.98)	0.77 (1.48)	1.28 (2.20)
0	Tangential	0.53 (0.74)	0.51 (0.81)	0.48 (0.85)	0.47 (0.92)
0	Axial	0.73 (1.62)	0.71 (1.46)	0.67 (1.42)	0.72 (1.44)
0	Volumetric	0.19 (0.91)	0.18 (1.16)	0.25 (1.78)	0.44 (2.91)
6.25	Radial	0.47 (0.77)	0.61 (1.05)	0.88 (1.60)	1.28 (2.03)
6.25	Tangential	0.45 (0.87)	0.55 (0.89)	0.47 (0.93)	0.52 (0.96)
6.25	Axial	0.64 (1.21)	0.70 (1.24)	0.65 (1.23)	0.53 (1.01)
6.25	Volumetric	0.13 (0.81)	0.23 (1.17)	0.27 (1.83)	0.35 (1.98)
13.5	Radial	0.39 (0.86)	0.59 (1.10)	0.83 (1.47)	1.26 (2.06)
13.5	Tangential	0.52 (0.82)	0.50 (0.84)	0.49 (0.87)	0.49 (0.97)
13.5	Axial	0.60 (1.04)	0.62 (1.09)	0.66 (1.17)	0.65 (1.20)
13.5	Volumetric	0.12 (0.73)	0.18 (1.01)	0.27 (1.50)	0.40 (2.40)
19.75	Radial	0.41 (0.85)	0.54 (0.92)	0.83 (1.36)	1.22 (1.89)
19.75	Tangential	0.45 (0.83)	0.55 (0.83)	0.46 (0.92)	0.56 (0.99)
19.75	Axial	0.37 (0.79)	0.36 (0.81)	0.42 (0.78)	0.49 (0.75)
19.75	Volumetric	0.07 (0.56)	0.11 (0.62)	0.16 (0.98)	0.34 (1.40)

SUPPLEMENTAL TABLE 5. The NEMA NU4 image quality phantom analysis results with the FBP and the OSEM.

Uniformity			Recovery coefficient			Spill-over ratio		
Parameter	OSEM	FBP	Rod	OSEM	FBP	Region	OSEM	FBP
Mean	1.00	1.00	1 mm	0.35±0.21	0.33±0.35	Water	0.10±0.06	0.16±0.05
Max	1.25	1.20	2 mm	1.01±0.11	0.58±0.18	Air	0.20±0.07	0.24±0.06
Min	0.82	0.77	3 mm	1.02±0.12	0.77±0.12			
%STD	6.38	6.26	4 mm	1.04±0.10	0.92±0.10			
			5 mm	1.06±0.10	1.00±0.10			

SUPPLEMENTAL TABLE 6. The Effect of Energy Window on the VPR of the Modified Ultra-Micro Hot Phantom With the OSEM.

	Energy window [keV]			
Rod dia. [mm]	250-750	350-650	400-600	440-560
0.75	0.711±0.069 (75%)	0.657±0.065 (91.7%)	0.611±0.065 (91.7%)	0.543±0.065 (100%)
1.0	0.435±0.060	0.394±0.031	0.343±0.040	0.257±0.047
1.35	0.266±0.078	0.223±0.053	0.187±0.054	0.136±0.041
1.7	0.190±0.052	0.156±0.019	0.124±0.017	0.091±0.014
2.0	0.172±0.045	0.136±0.032	0.109±0.026	0.074±0.017
2.4	0.135±0.044	0.109±0.020	0.080±0.014	0.058±0.008
Sensitivity [%]	8.66	4.39	2.84	1.56
Prompt count	157,473,109	71,755,919	43,169,157	22,478,487

The resolvability is given in parentheses only for the 0.75 mm rod diameter as it was 100% for all others.

SUPPLEMENTAL Table 7. The VPRs of the SPECT Rat Phantom and PET Mouse Phantom with the OSEM.

Phantom	SPECT Rat phantom	PET Mouse phantom	
Rod [mm]	VPR (Resolvability)	Rod [mm]	VPR (Resolvability)
0.7	0.629±0.075 (100%)	0.45	0.847±0.066 (8%)
0.8	0.449±0.041 (100%)	0.5	0.730±0.047 (55.5%)
0.9	0.340±0.051 (100%)	0.55	0.527±0.077 (100%)
1.0	0.284±0.046 (100%)	0.75	0.254±0.039 (100%)
1.2	0.181±0.040 (100%)	0.8	0.279±0.054 (100%)
1.5	0.138±0.034 (100%)	0.85	0.241±0.019 (100%)
Prompt	48,674,500		23,945,839
Random	2,527,007		655,080

The resolvability is shown inside the parenthesis.